

---

**Supplementary information**

---

**Correlative operando microscopy of oxygen evolution electrocatalysts**

---

In the format provided by the  
authors and unedited

## SUPPLEMENTARY INFORMATION

### **Correlative *operando* microscopy of oxygen evolution electrocatalysts**

J. Tyler Mefford,<sup>1,2,\*</sup> Andrew R. Akbashev,<sup>1,2</sup> Minkyung Kang,<sup>3</sup> Cameron L. Bentley,<sup>3</sup> William E. Gent,<sup>1</sup> Haitao D. Deng,<sup>1</sup> Daan Hein Alsem,<sup>4</sup> Young-Sang Yu,<sup>5</sup> Norman J. Salmon,<sup>4</sup> David A. Shapiro,<sup>5</sup> Patrick R. Unwin,<sup>3</sup> William C. Chueh<sup>1,2,\*</sup>

<sup>1</sup>*Department of Materials Science and Engineering, Stanford University, Stanford, CA 94305, USA.*

<sup>2</sup>*Stanford Institute for Materials and Energy Sciences, SLAC National Accelerator Laboratory, Menlo Park, CA 94025, USA.*

<sup>3</sup>*Department of Chemistry, University of Warwick, Coventry CV4 7AL, U.K.*

<sup>4</sup>*Hummingbird Scientific, Lacey, WA 98516, USA.*

<sup>5</sup>*Advanced Light Source, Lawrence Berkeley National Laboratory, Berkeley, CA 94720, USA.*

\*Correspondence to: [tmefford@stanford.edu](mailto:tmefford@stanford.edu); [wchueh@stanford.edu](mailto:wchueh@stanford.edu)

## Supplementary Information Table of Contents

<b>Table of Contents</b> .....	<b>S2</b>
<b>Methods</b> .....	<b>S3 – S16</b>
<i>Synthesis of <math>\beta</math>-Co(OH)<sub>2</sub> platelet particles:</i> .....	S3
<i>Synthesis of Sr<sub>6</sub>Co<sub>5</sub>O<sub>15</sub> (“Co<sup>3.6+</sup>”) Co L<sub>III</sub>-edge reference compound:</i> .....	S3
<i>Electron Microscopy Imaging:</i> .....	S3
<i>Optical Imaging:</i> .....	S3
<i>Electrochemical Instrumentation:</i> .....	S3
<i>Rotating Disk Electrochemistry:</i> .....	S4
<i>Scanning Electrochemical Cell Microscopy:</i> .....	S4 – S5
<i>Electrochemical Atomic Force Microscopy:</i> .....	S6
<i>Electrochemical Quartz Crystal Microbalance:</i> .....	S7 – S8
<i>Operando Scanning Transmission X-ray Microscopy Instrumentation:</i> .....	S8 – S9
<i>Statistical comparison of voltage-dependent STXM phasemaps and STXM-XAS derived Co oxidation state</i> .....	S9 – S10
<i>STXM Spectro-Image Processing and Principal Component Analysis/Non-negative Matrix Factorization:</i> .....	S10 – S16
<i>UV-Vis Spectroelectrochemistry:</i> .....	S16
<i>Powder X-ray Diffraction:</i> .....	S16
<b>Supplementary Discussion</b> .....	<b>S17 – S24</b>
<i>Is Co<sup>4+</sup> Present during the OER in the CoO<sub>x</sub>H<sub>y</sub> System?</i> .....	S17 – S18
<i>Co L-edge versus K-edge XAS for Oxidation State Assignment:</i> .....	S18
<i>UV-Vis Spectroelectrochemistry:</i> .....	S18 – S19
<i>Window Bowing:</i> .....	S19 – S20
<i>Radiation Effects:</i> .....	S21 – S23
<i>Ex-situ STXM and XRD analysis of relaxed <math>\beta</math>-Co(OH)<sub>2</sub> particles after oxidation:</i> .....	S23
<b>Supplementary References</b> .....	<b>S24 – S26</b>

## Methods:

### *Synthesis of $\beta$ -Co(OH)<sub>2</sub> platelet particles:*

$\beta$ -Co(OH)<sub>2</sub> platelet particles were synthesized as previously described.<sup>6</sup> In short, a 400 mL aqueous solution of 45 mM hexamethylenetetramine (HMT,  $\geq 99.0\%$ , SigmaAldrich) was brought to 85 °C with magnetic stirring under N<sub>2</sub> atmosphere. 3.5 mmol of CoCl<sub>2</sub>·6H<sub>2</sub>O (98%, SigmaAldrich) dissolved in 20 mL ultrapure de-ionized water (“DI water”, 18.2 M $\Omega$  cm resistance, MilliQ) was added dropwise to the HMT solution and allowed to reflux under continuous magnetic stirring and nitrogen protection for 5 hours. The stirring was then stopped and the solution was allowed to cool to room temperature naturally under N<sub>2</sub> atmosphere. The precipitate was collected through centrifugation and washed with DI water and anhydrous ethanol, in turn, then dried overnight in an 80 °C oven.

### *Synthesis of Sr<sub>6</sub>Co<sub>5</sub>O<sub>15</sub> (“Co<sup>3.6+</sup>”) Co L<sub>III</sub>-edge reference compound:*

Stoichiometric amounts of Sr(NO<sub>3</sub>)<sub>2</sub> ( $\geq 99.0\%$ , SigmaAldrich) and Co(NO<sub>3</sub>)<sub>2</sub>·6H<sub>2</sub>O (99.999%, SigmaAldrich) were dissolved in 100 mL of DI water such that the total concentration of metal ions was 0.1 M. 10 mmol of citric acid ( $\geq 99.5\%$ , SigmaAldrich) and 636  $\mu$ L of diethylene glycol ( $\geq 99.0\%$ , SigmaAldrich) were added and the mixture was stirred at 85 °C on a hotplate until the water evaporated. The resulting gel was heated at 350 °C to decompose the polymer. The resulting mixed-metal oxide powder was heated in a tube furnace with a 1 h ramp to 120 °C, 1 h hold at 120 °C, 1 h ramp to 950°C, and 5 h hold at 950 °C under 200 mL min<sup>-1</sup> O<sub>2</sub> then allowed to cool to room temperature naturally. The product was washed with water followed by ethanol, collected through sonication at 6000 rpm for 5 min, and dried overnight in an oven at 80 °C. The purity and structure were confirmed through powder X-ray diffraction.

### *Electron Microscopy Imaging:*

Scanning electron microscopy (SEM) was performed on a FEI XL30 Sirion SEM with FEG source with secondary electron collection, an acceleration voltage of 5 kV, and beam current of 20 pA.  $\beta$ -Co(OH)<sub>2</sub> particles were dispersed in ethanol and dropcast on flat <100> Si substrates (Ted Pella Inc.). Transmission electron microscopy (TEM) was performed in bright-field mode using an aberration-corrected Titan ETEM 80-300 operated at 300 kV in ultra-high vacuum.

### *Optical Imaging:*

Optical microscopy was performed using a Leica DM4000 M in brightfield mode.

### *Electrochemical Instrumentation:*

Electrochemical control during the EC-AFM, EQCM, and *operando* STXM was performed using an SP-300 potentiostat (BioLogic). Rotating disk electrochemistry (RDE) and UV-Vis spectroelectrochemistry was performed using a VSP-300 potentiostat (Biologic). SECCM electrochemistry was performed using home-built instrumentation as described below. All voltages are referenced versus the reversible hydrogen electrode (RHE), where the RHE potential of the reference electrodes for each experiment was standardized against a bulk RHE electrode (Hydroflex Hydrogen Reference Electrode, eDAQ) in 0.1 M KOH prior to testing.

### *Rotating Disk Electrochemistry:*

RDE characterization was performed as previously described.<sup>6</sup> 9.8  $\mu\text{L}$  of ink solutions containing 3:1 DI water:IPA, 0.05 wt% Na-substituted Nafion (prepared from 5 wt% Nafion 117 in lower alcohols, SigmaAldrich, Na-substitution described elsewhere<sup>32</sup>), and 1, 0.5, or 0.2  $\text{mg mL}^{-1}$   $\beta\text{-Co(OH)}_2$  were dropcast on PTFE shrouded glassy carbon (GC) rotating disk electrodes ( $0.196 \text{ cm}^2_{\text{geom}}$  area, E3 series, Pine Research Instrumentation) and allowed to dry naturally under a scintillation vial overnight to yield electrode loadings of 50, 25, and 10  $\mu\text{g cm}^{-2}_{\text{geom}}$ , respectively. The GC electrodes were cleaned and polished to a mirror finish prior to dropcasting by, in order, sonication in a 1:1 IPA:DI water solution for 5 minutes, polishing with a slurry of de-agglomerated 50 nm alumina spheres in water (Allied High Tech Products, Inc.) on a nylon polishing pad (Buehler), vigorous rinsing with DI water, sonication in a 1:1 IPA:DI water solution for 5 minutes, and drying under vigorous  $\text{N}_2$  flow. Scan rate dependent cyclic voltammetry was performed using a rotation rate of 1600 rpm (MSR Rotator, Pine Research Instrumentation) between 1.0 – 1.75 V vs. RHE. Uncompensated resistance,  $R$ , was measured through electrochemical impedance spectroscopy at the high frequency intercept ( $f > 1 \text{ kHz}$ , phase angle =  $0^\circ$ ) and  $iR$  correction was performed manually during data workup. All RDE tests were performed in an alkaline resistant PTFE cell (AF01CKT1001, Pine Research Instrumentation) using an electrolyte of  $\text{O}_2$  saturated 0.1 M KOH (99.99%, Semiconductor Grade, SigmaAldrich), a polyether ether ketone (PEEK) shrouded/polymeric frit leakless Ag/AgCl reference electrode (ET069, Leakless Ag/AgCl, eDAQ), and a coiled Pt wire as the counter electrode. Control experiments regarding the role of Fe-contamination in the electrolyte were performed using Fe-purified 0.1 M KOH prepared through the  $\text{Ni(OH)}_2$  precipitation protocol by Trotochaud et al.<sup>33</sup> and in “Fe-spiked” 0.1 M KOH prepared through the addition of 1 mM  $\text{Fe(NO}_3)_3 \cdot 9\text{H}_2\text{O}$  (98+%, SigmaAldrich) following the protocol by Burke Stevens *et al.*<sup>34</sup> No variation in the electrochemistry (redox peak voltages and OER current) was observed compared to unpurified 0.1 M KOH (99.99%, Semiconductor Grade, SigmaAldrich).

### *Scanning Electrochemical Cell Microscopy:*

The substrate electrode was prepared by dropcasting 3 ml of  $\beta\text{-Co(OH)}_2$  ink, containing 2 mg of  $\beta\text{-Co(OH)}_2$  particles in 2 ml tetrahydrofuran, on a freshly cleaned GC plate (HTW-Germany). After allowing the ink to dry on the GC surface, the dropcast area was gently stamped with a clean PDMS block to remove agglomerated particles. The prepared substrate was then covered with a thin layer of dodecane (> 99%, MERCK), a nonpolar and a very low dielectric medium, which served to prevent leakage of the nanoscale droplet during SECCM mapping.<sup>35</sup> The micropipette probe was fabricated from a quartz theta capillary (Outer Diameter = 1.2 mm; Inner Diameter = 0.9 mm, Friedrich & Dimmock, Inc.) with a  $\text{CO}_2$ -laser puller (P-2000, Sutter Instruments) and characterized with FE-SEM (GeminiSEM, ZEISS). The probe (tips) possessed  $d_{\text{tip}}$  of  $\sim 400 \text{ nm}$  for the scanning mode experiments and  $\sim 440 \text{ nm}$  for the hopping mode experiments. This specific  $d_{\text{tip}}$  was chosen in order to ensure full encapsulation of both the edge of the  $\beta\text{-Co(OH)}_2$  particles and the GC support with the meniscus (droplet) cell, while ensuring sufficient spatial resolution (sub-500 nm, herein) to distinguish edge sites from the basal surface of the particles.<sup>11</sup> SECCM is a well-established technique and the experimental set up has been fully described in previous studies.<sup>11,36–38</sup> In brief, after preparing the micropipette as described above, both channels were filled with 0.1 M KOH and fitted with a quasi-reference counter electrode (QRCE; e.g., AgCl coated Ag wire). The meniscus (droplet) cell used to interrogate the

substrate working electrode forms naturally at the end of the filled micropipette probe. The prepared micropipette and substrate were mounted on z- and xy-piezoelectric positioners (P-753.3CD and P-622.2CD, PhysikInstrumente), respectively, for nanoscale translocations in three-dimensional (3D) space.

During operation of the hopping experiments, a voltage of 50 mV ( $V_1$ ) was applied between two QRCEs, inducing ionic current flow ( $I_{ion}$ , ~500 pA) across the meniscus, between the two barrels of the pipette.  $I_{ion}$  was constantly monitored throughout the scan (using a home-built current amplifier) and served as a feedback signal to precisely position the meniscus (droplet) cell to the substrate electrode. A change in magnitude of 30 pA was utilized as a feedback set point for  $I_{ion}$ . Note that the micropipette itself did not physically contact the substrate. Upon registering meniscus-substrate contact, the probe ceased translation and an LSV was recorded at a voltammetric scan rate of  $1 \text{ V s}^{-1}$ , from 1.1 to 1.8 V vs RHE. This was achieved by linearly sweeping  $V_2$ . The working electrode voltage is  $-(V_2 + V_1/2)$ .<sup>39</sup> The electrochemical current ( $I_{WE}$ ) was measured at the substrate with a home-built current amplifier. All data including both  $I_{ion}$  and  $I_{WE}$  was recorded every 4  $\mu\text{s}$ , which was averaged 512 times, to give a data acquisition rate of  $4 \times (512 + 1) = 2052 \mu\text{s}$  per point (note that one extra iteration is used to transfer the data to the host computer). An FPGA card (PCIe-7852R, National Instruments) controlled by a LabVIEW 2016 (National Instruments) interface running the Warwick Electrochemical Scanning Probe Microscopy (WEC-SPM, [www.warwick.ac.uk/electrochemistry](http://www.warwick.ac.uk/electrochemistry)) software was utilized to achieve fast data acquisition and fine control of the instrument (piezoelectric positioners and applied voltages to the SECCM cell).

Individual LSVs (660 different positions on the surface for the data in Figure 2) and the position of micropipette probe in 3D space, recorded throughout the scan, were processed with MATLAB 2018 (Mathworks) to produce spatially resolved topography and electrochemical data.  $I_{WE}(V_2, x, y)$  was used to obtain equipotential images of the current and a movie of electrochemical activity as a function of voltage (Supplementary Movie S1).

For scanning mode experiments, line scans over individual  $\beta\text{-Co(OH)}_2$  particles were conducted at constant tip-particle distance at a fixed potential of 1.87 V vs. RHE. During scanning, the Z position of the micropipette probe was modulated (amplitude = 40 nm, frequency = 327 Hz) by implementing an AC signal generated by a lock-in amplifier (SR830, Stanford Research Systems) to generate a sensitive AC feedback signal for positioning (using a feedback setpoint of 8 pA amplitude).<sup>40</sup> The lateral translation rate of the probe was  $30 \text{ nm s}^{-1}$ .

We note that the unique nanodroplet configuration of SECCM allows for rapid and efficient gas exchange across the liquid-air<sup>41</sup> or liquid-liquid (e.g. oil-water)<sup>42</sup> interface. Thus, SECCM is relatively immune to the complications normally associated with gas bubble formation at macroscopic electrode/electrolyte interfaces as gaseous products simply escape across the liquid-air or liquid-liquid phase boundary. It has previously been shown that current densities in excess of  $500 \text{ mA cm}^{-2}$  can be passed during hydrogen evolution in the SECCM configuration without any consequence of gas bubble formation.<sup>11,43,44</sup>

## Electrochemical Atomic Force Microscopy:

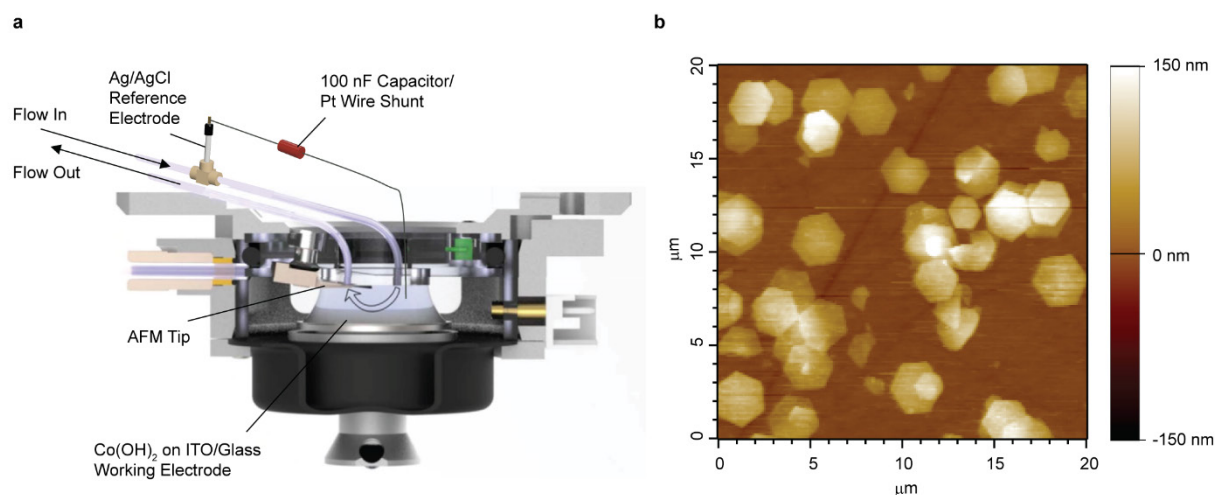


**Figure S1 | Operando EC-AFM (a)** Operando EC-AFM Cell. The electrochemical cell makes use of a capacitive shunt between a Ag/AgCl reference electrode that is outside of the cell and an electrically floating (unbiased) Pt wire in the electrolyte. This allows us to bypass the RC time constant effects caused by the high resistance of the ionic pathway between the external reference electrode and the working/counter electrodes. The working electrode is ITO/glass with a sub-monolayer coverage of  $\beta$ -Co(OH)<sub>2</sub> particles such that individual particles can be addressed during the operando measurements. The counter electrode is a Pt ring located at the top of the cell. The cell can operate with flow but in general the flow is used only to maintain sufficient electrolyte in the small volume cell. **(b)** AFM image with a wide field of view of the working electrode. During the operando measurements, a single particle is interrogated.

EC-AFM samples were prepared similarly to the SECCM experiments using 1 x 1 cm<sup>2</sup> ITO/glass substrates (MSE Supplies) in place of GC substrates (Figure S1b). EC-AFM was performed in tapping mode using a Cypher ES scanning probe microscope (Oxford Instruments Asylum Research Inc.). To ensure high voltage referencing stability, a 100 nF capacitive Pt wire shunt was connected in parallel to the leakless Ag/AgCl reference electrode (Figure S1a). During topography scans, Olympus AC55TS tips (radius  $\sim$ 7 nm) were excited photothermally (blueDrive<sup>TM</sup>) on the gold-coated reflex side at the resonance frequency of approximately 1 MHz in 0.1 M KOH. To ensure the tip probed the surface in a repulsive regime but did not mechanically induce changes in the samples, the phase was kept close to 70-80° (free-liquid phase was 90°). Linear sweep voltammetry was performed at a scan rate was 5 mV min<sup>-1</sup>. Each topography map (frame) was collected in 642 s (10.7 min), having a size of 1 x 1  $\mu$ m<sup>2</sup> and containing 512 x 512 pixels (1.95 nm step size). A long collection time for each frame avoided a “parachuting” effect and enabled a precise tracking of the particles’ edges for size determination. Electrolyte was flowed into and withdrawn from the cell using two separate syringe pumps (PHD ULTRA, Harvard Apparatus) at a rate of 50-70  $\mu$ L min<sup>-1</sup>.

The Asylum software package implemented into Igor Pro was used for flattening the AFM images. Each AFM image was aligned to the image at the open-circuit voltage (0.96 V) and plotted using MATLAB 2018. Differential height images represent the image at a selected voltage subtracting the initial open-circuit voltage image.

## Electrochemical Quartz Crystal Microbalance:

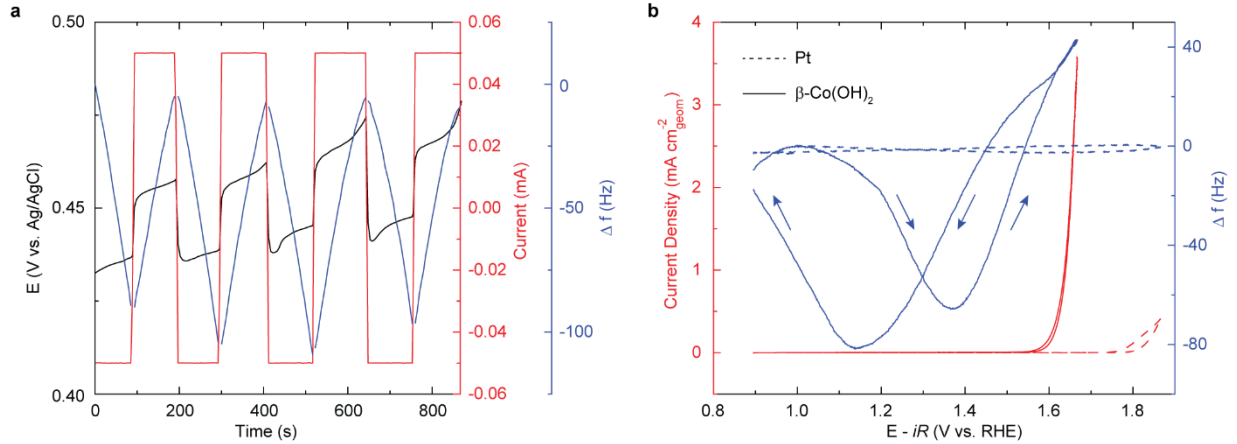


**Figure S2 | Electrochemical quartz crystal microbalance calibration and  $\beta\text{-Co(OH)}_2$  measurements** (a) Isothermal calibration of Pt EQCM crystal through galvanostatic Ag deposition/stripping using current of  $\pm 50 \mu\text{A}$  and electrolyte  $0.05 \text{ M AgNO}_3$  in  $0.5 \text{ M HNO}_3$  and  $T = 25^\circ\text{C}$ . The measured Sauerbrey constant,  $C_f$ , of the Pt-coated quartz  $5 \text{ MHz}$  crystal was  $45 \pm 2 \text{ Hz } \mu\text{g}^{-1} \text{ cm}^2$ . (b) Isothermal EQCM cyclic voltammetry of  $100 \mu\text{g cm}^{-2} \text{ Co(OH)}_2/30 \mu\text{g cm}^{-2}$  Na-substituted Nafion on Pt-coated quartz EQCM electrode (solid lines) in  $0.1 \text{ M KOH}$  at scan rate of  $v = 5 \text{ mV min}^{-1}$ . Included are the current and frequency changes for a  $30 \mu\text{g cm}^{-2}$  Na-substituted Nafion on Pt-coated quartz EQCM electrode ( $\text{Co(OH)}_2$  free, dashed lines) tested under identical conditions.

EQCM was performed using a QCM200 Quartz Crystal Microbalance (Stanford Research Systems) with  $5 \text{ MHz}$  titanium/platinum quartz crystal electrodes (O100RX4, Stanford Research Systems). Prior to electrochemical testing, and  $\beta\text{-Co(OH)}_2$  electrode preparation, the EQCM electrodes were cleaned by successive sonication in ethanol, isopropanol, and DI water for 5 minutes each. Calibration of the electrodes was performed by galvanostatic Ag plating/stripping experiments at currents of  $\pm 50 \mu\text{A}$  in a  $50 \text{ mM AgNO}_3$  in  $0.5 \text{ M HNO}_3$  electrolyte (Figure S2) while monitoring the resonant frequency change ( $\Delta f$ ) of the electrode (alternating between plating and stripping when  $|\Delta f| \approx 75\text{-}100 \text{ Hz}$ ). The relationship between the frequency change,  $\Delta f$ , and mass change,  $\Delta m$ , is described by the Sauerbrey equation:<sup>45</sup>

$$\Delta f = -\frac{2f_0^2}{A\sqrt{\rho\mu}}\Delta m \quad (\text{S1})$$

where  $f_0$  is the nominal frequency of the crystal ( $5 \text{ MHz}$ ),  $A$  is the area of the piezo active region ( $0.38 \text{ cm}^2$ ), and  $\rho$  and  $\mu$  are the density and shear modulus of an AT-cut quartz crystal, respectively. For a standardized EQCM electrode, Equation S1 can be simplified as (where  $C_f$  is the Sauerbrey constant):

$$\Delta f = -C_f\Delta m \quad (\text{S2})$$

Assuming  $1 \text{ e}^-/\text{Ag}$  atom deposited, the calibrated  $C_f$  was found to be  $45 \pm 2 \text{ Hz } \mu\text{g}^{-1} \text{ cm}^2$ , where the error represents the single standard deviation of 4 plating/stripping experiments.

$\beta\text{-Co(OH)}_2$  electrodes were prepared by spincoating (WS-650-23NPPB, Laurell Technologies Corporation) at a mass loading of  $100 \mu\text{g cm}^{-2}_{\text{geom}}$   $\beta\text{-Co(OH)}_2$  with  $30 \mu\text{g cm}^{-2}_{\text{geom}}$  Na-substituted Nafion onto titanium/platinum QCM electrodes (electrochemically active area =  $1.37 \text{ cm}^2$ ). Electrodes were also prepared with only  $30 \mu\text{g cm}^{-2}_{\text{geom}}$  Na-substituted Nafion

(without  $\beta$ -Co(OH)<sub>2</sub>) by the same method. EQCM experiments were performed using cyclic voltammetry at a scan rate of 5 mV min<sup>-1</sup> between 1.0 – 1.8 V vs. RHE (non-*iR* corrected). Uncompensated resistance was measured through electrochemical impedance spectroscopy at the high frequency intercept and *iR* correction was performed manually during data workup.

All EQCM experiments (calibration and  $\beta$ -Co(OH)<sub>2</sub>) were performed isothermally (*T* = 25 °C) in a jacketed beaker (Chemglass CG-1103-04) cooled by recirculating water (NESLAB RTE-7, Thermo Scientific) using a leakless Ag/AgCl reference electrode (ET069, Leakless Ag/AgCl, eDAQ) and coiled Pt wire counter electrode.

#### *Operando Scanning Transmission X-ray Microscopy Instrumentation:*

*Operando* STXM was performed at Beamline 11.0.2.2 at the Advanced Light Source at Lawrence Berkeley National Lab using a custom designed electrochemical flow cell manufactured by Hummingbird Scientific.

The general layout of the cell is presented in Figure S3a,b and is based on a sandwiched design of two patterned Si chips. One chip, not shown, provides the platform for the flow channel. It is patterned with 100 nm thick SiO<sub>2</sub> ridges on the top and bottom edges leaving a central channel open. In the middle of this channel is a 100 nm thick SiN<sub>x</sub> window. The second chip patterned with Pt shunt (SE) and counter electrodes (CE) and either Pt or indium tin oxide (ITO) working electrodes (WE) patterned on top of a 100 nm thick SiN<sub>x</sub> window, shown in Figure S3c, serves as the substrate to investigate the electrochemistry of the  $\beta$ -Co(OH)<sub>2</sub> particles. The  $\beta$ -Co(OH)<sub>2</sub> particles are dropcast onto the electrode chip and then stamped with a piece of polydimethylsiloxane (PDMS) to leave a sub-monolayer coverage of isolated  $\beta$ -Co(OH)<sub>2</sub> particles. Particle loadings were on the order of 1-10 x 10<sup>6</sup> particles cm<sup>-2</sup><sub>WE</sub> (0.7 – 7  $\mu$ g cm<sup>-2</sup><sub>WE</sub>). An external Ag/AgCl reference electrode was used, which was connected outside of the cell through the fluidic inlet tubing. A 100 nF capacitor connected in parallel between the reference electrode and a floating Pt shunt electrode on the electrode chip was used to bypass the resistive effects due to the small inner diameter fluidic tubing (360  $\mu$ m) which can cause potentiostat instability due to phase shifts of the voltage controller operational amplifier. Uncompensated resistances measured through the current interrupt method were generally on the order of 10-50 k $\Omega$ .

The spectro-microscopy and oxidation state of the particles was measured at steady-state voltages at long times (>1 h). Because of this it was imperative that the cell have high fidelity in the voltage control and measurement. Validation of the cell was performed by investigating the electrochemistry of a fast reversible redox couple, 10 mM Fe(CN)<sub>6</sub><sup>3-</sup>/10 mM Fe(CN)<sub>6</sub><sup>4-</sup> in 0.1 M KOH, and comparing the results to those obtained in a macroscopic RDE cell using a GC electrode, as shown in Figure S3g. There are no spurious ground loops or voltage offsets when measuring the Fe(CN)<sub>6</sub><sup>3-</sup>/Fe(CN)<sub>6</sub><sup>4-</sup> redox couple. The STXM cell shows a well-behaved sigmoidal shape reflecting the high mass transfer rate in the cell compared to the slow scan rate of  $\nu = 1$  mV s<sup>-1</sup>. The RDE results, where the electrode was not rotated, shows the typical “duck-shaped” voltammograms characteristic of diffusion-controlled mass transfer to the electrode surface. Equivalent results were obtained whether the working electrode on the electrode chip was patterned with Pt or ITO. We therefore have high confidence that the STXM data does indeed depict the electronic states of the particles at the specified voltages. The robust

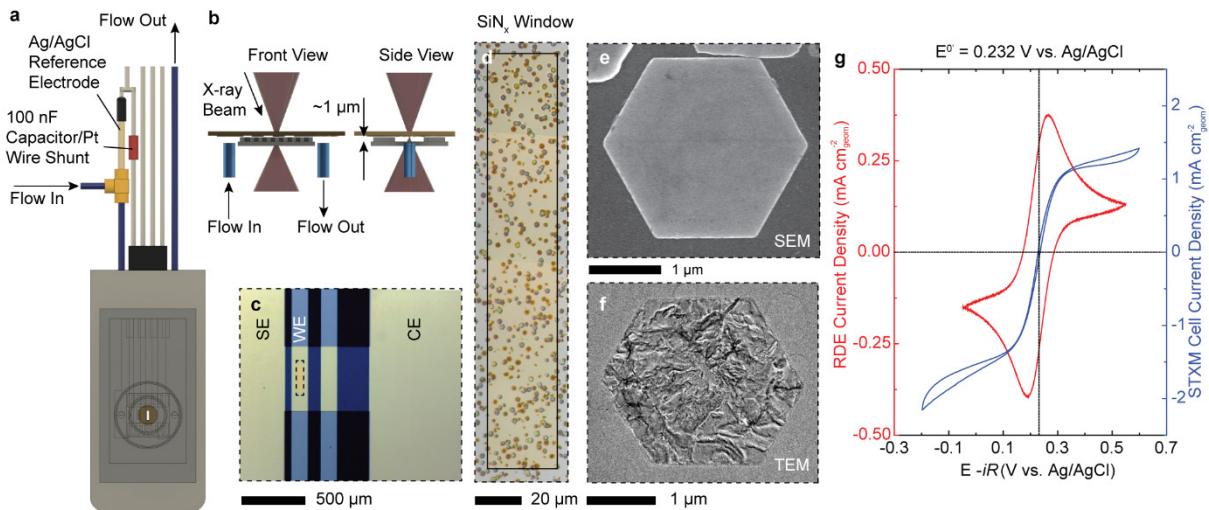


**Figure S3 | Operando STXM Cell and Electrochemical Validation** (a) STXM flow cell setup. The cell is based on a sandwiched design using a spacer chip with a 100 nm thick  $\text{SiN}_x$  window compressed on an electrochemical chip with a 100 nm thick  $\text{SiN}_x$  window on the working electrode. The spacer chip is patterned with a flow channel to allow electrolyte to flow passed the electrodes and the windows. (b) Views of the sandwiched configuration of the spacer and electrode chips showing the X-ray beam and electrolyte flow paths. (c) Magnified view of the electrodes on the electrochemical chip. The chip is patterned with four electrodes (although only the three labeled are used in this study). The shunt (SE) and counter (CE) electrodes are patterned with Pt and the working electrode (WE) is patterned with either Pt or ITO on top of a 100 nm thick  $\text{SiN}_x$  window. The working electrode (area =  $4.5 \times 10^{-5} \text{ cm}^2$ ) with the  $\text{SiN}_x$  window is centered on the chip and the  $\text{Co(OH)}_2$  platelet particles are dropcast on this electrode. (d) Magnified view of the  $\text{SiN}_x$  window covered with a Pt coated working electrode with dropcast isolated  $\text{Co(OH)}_2$  particles. (e) SEM image and (f) TEM image of single  $\text{Co(OH)}_2$  particles on the  $\text{SiN}_x$  window. (g) Cyclic voltammograms of 10 mM  $\text{K}_3\text{Fe(CN)}_6$ /10 mM  $\text{K}_4\text{Fe(CN)}_6$  in 0.1 M KOH on a glassy carbon electrode in a macroscopic cell (RDE setup, red) at a scan rate of  $\nu = 10 \text{ mV s}^{-1}$  with no rotation and in the operando STXM cell (blue) at a scan rate of  $\nu = 1 \text{ mV s}^{-1}$  and a flow rate of  $10 \mu\text{L min}^{-1}$ . The RDE shows the typical “duck-shaped” voltammogram as it was not rotated while the STXM shows a sigmoidal voltammogram due to the slow scan rate and the effective mass transfer due to flow.  $E_{1/2}$  is centered at the reversible redox potential for both cells showing the high electrochemical fidelity of the operando STXM cell using an external Ag/AgCl reference electrode coupled to a capacitive shunt.

electrochemistry highlights a key benefit of liquid cell X-ray microscopy, where the longer attenuation length of X-rays compared to electrons allows for  $\sim 10\times$  thicker electrolyte over the particles than the 100 nm liquid layer thicknesses typically needed for imaging in liquid cell TEM.<sup>46</sup>

#### Statistical comparison of voltage-dependent STXM phasemaps and STXM-XAS derived Co oxidation state

To ensure steady-state behavior of the particles, multiple particles were measured during the potentiostatic STXM experiments, as shown in Figure S4. The results show similar distributions in oxidation states across the pixels in the phasemaps of the particles, verifying the particles have reached their steady-state behavior. The average oxidation state of

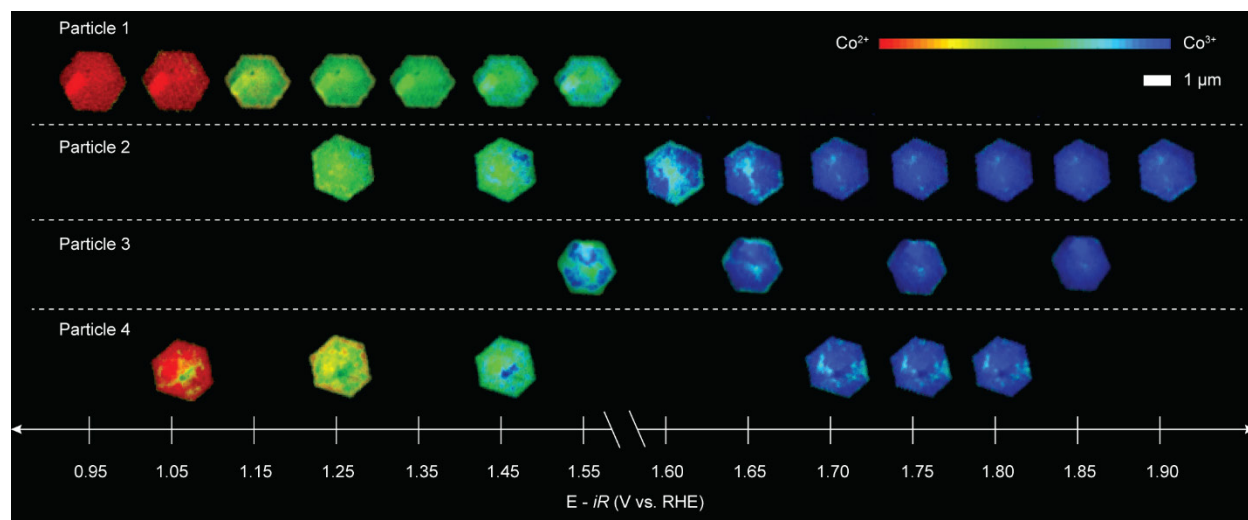


**Figure S4 | STXM Co oxidation state phasemaps of all particles reported in this study.** For most voltages there are multiple particles measured. These particles show similar distributions in oxidation states and their average oxidation states and single pixel oxidation state standard deviations are used in the ideal solution model analysis.

the particles and single standard deviation of the single-pixel oxidation states were used in the ideal solution modeling of the electrochemical behavior of  $\beta$ -Co(OH)<sub>2</sub>.

#### *STXM Spectro-Image Processing and Principal Component Analysis/Non-negative Matrix Factorization:*

Each scanning transmission x-ray microscopy spectro-image is collected as a stack of images collected at a single x-ray photon energy. Each image consists of pixels corresponding to the number of transmitted photons at that energy. The pixel size is determined by the zone-plate dimensions and the step size of the interferometer controlled piezoelectric stage, in this case 45 nm for the zone plate and a 50 nm step size. By taking images at discrete energies spanning an absorption edge, such as the Co L<sub>III</sub>-edge used in this study, the stack of images can be constructed into an  $[x, y, I_E]$  matrix, where  $x$  and  $y$  correspond to the position of the pixel and  $I_E$  corresponds to the number of photons transmitted in the pixel at a given energy. The stacks are first aligned (i.e. the  $[x, y, I_E]$  pixels are shifted in  $x$  and  $y$ ) using the aXis2000 software to account for drift of the piezo and x-ray focus over the time required to take the image stack, on the order of 30 minutes. To convert these raw transmission image stacks to absorbance, a cluster of pixels from a region of the image where there is no sample is averaged to obtain a background  $I_0$  spectrum for all energies. This process is repeated for each individual image stack collected for the entire set of *operando* STXM data. The images are then processed according to  $-\ln(I/I_0)$  for each single pixel absorbance spectrum yielding the full spectro-image.

To obtain average absorption spectra, the aligned absorbance image stacks are filtered at an energy of non-zero intensity, in this case 780.2 eV corresponding to the isosbestic point in the Co L<sub>III</sub>-edge spectra of Co<sup>2+</sup> and Co<sup>3+</sup>. A threshold is set for the absorbance of single pixels at this energy, generally  $< 0.1$  (corresponding to over 90% of the photons transmitted), and the pixels below this threshold were set to zero. This is necessary due to changes in absorbance by the electrolyte across an image caused by the bowing of the SiN<sub>x</sub> windows but does not significantly influence the analysis of the absorbance by the particles (Figure S9). A description

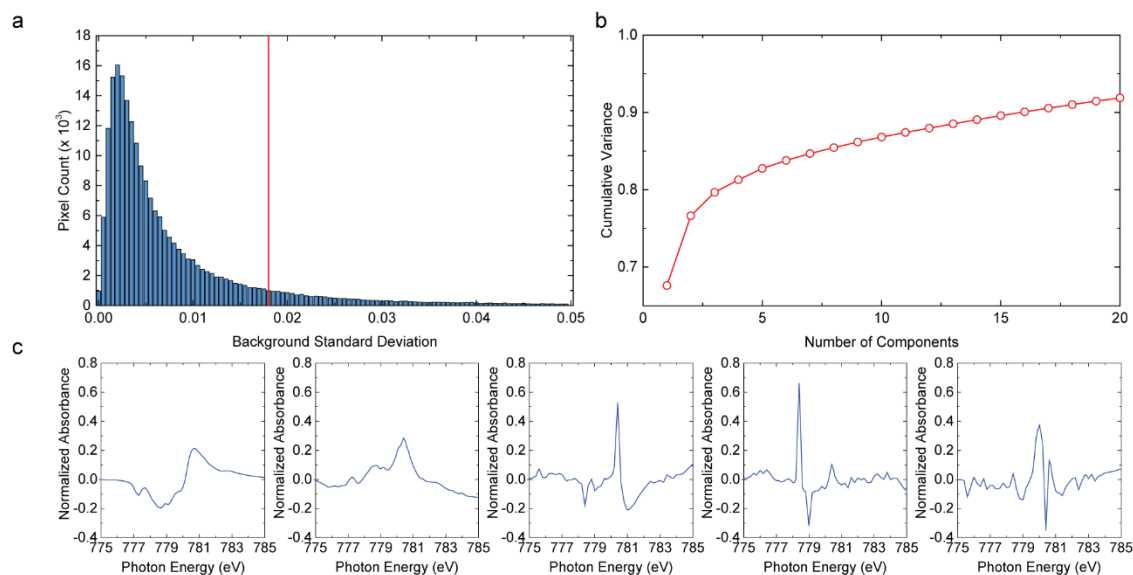


**Figure S5 | PCA and NMF Summary** (a) Histogram of the standard deviation in the background region for the Co spectro-images taken at all voltages with cutoff point indicated in red. (b) Cumulative variance of the first 20 principal components obtained by PCA. (c) The first five principal components.

of the window bowing is discussed in the Supplementary Information. The remaining pixels are then summed across the image to yield the average image spectrum. Normalization of this spectrum was done by subtracting the background intensity and then dividing by the integrated area of the full Co-L<sub>III</sub> edge.

As spectra obtained at high voltages are expected to be non-equilibrium states for which there may not be isolated reference spectra, we first analyze the full *operando* STXM data set using principal component analysis (PCA). The data is preprocessed by compiling every pixel of the spectro-images taken at all voltages into a single matrix of ~191,000 pixels x 118 energy points spanning the Co L<sub>III</sub>-edge from 774 – 785.7 eV. Offsets due to variations in the X-ray energy calibration between experiments were accounted for using a reference of pristine  $\beta$ -Co(OH)<sub>2</sub>. Each pixel was normalized by subtracting the mean background intensity (774 – 776 eV) and then dividing by the integrate L<sub>III</sub>-edge area.

After normalization, the data was filtered by removing data points with relatively large amounts of noise (as measured by standard deviation) in the background region (774 - 776 eV). A cutoff of 10% of the data with the highest standard deviation was used, as shown in Extended Figure 6a. This served to remove the pixels that originally had very low signal but were amplified by the normalization procedure. The data was then mean centered at each energy.

We then performed PCA on the data using the singular value decomposition (SVD) method.<sup>47</sup> Figure S5b shows the cumulative variance explained by the first 20 principal components identified by PCA. The first two components show the largest gain in cumulative variance, explaining ~77% of the total observed variance. As seen in Figure S5c, the first five components appear to contain more information than just noise, but components 3-5 show a

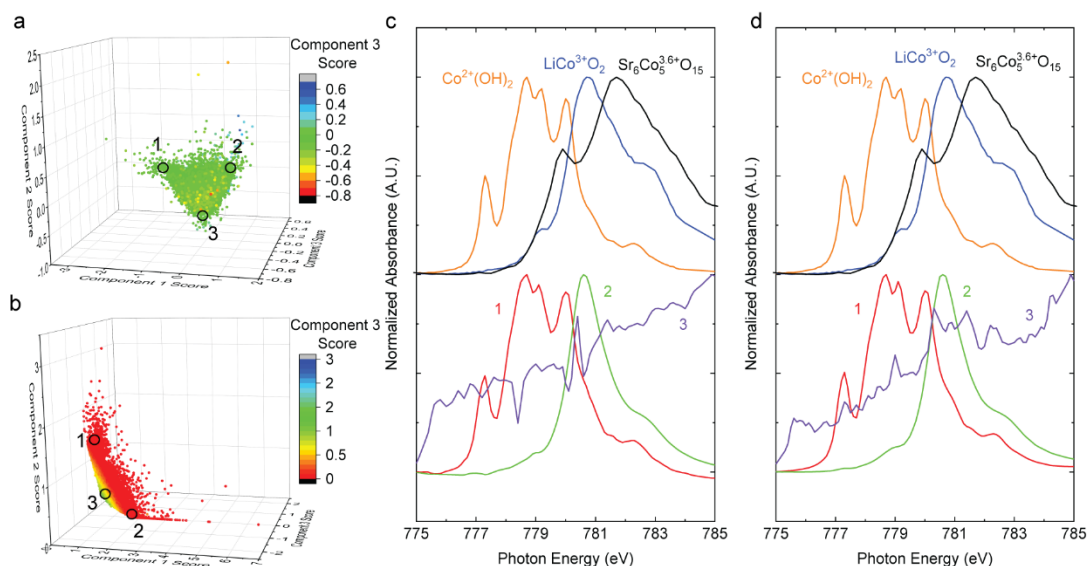


**Figure S6 | PCA and NMF End Members** (a) Plot of the operando STXM data in PCA space using the first three principal components. The color map corresponds to the component 3 score. (b) Plot of the same data in NMF space using the first three NMF components. (c) End member PCA derived spectra from the cluster averaged circled regions in (a) compared to reference spectra of pristine  $\beta\text{-Co(OH)}_2$  ( $\text{Co}^{2+}$ ),  $\text{LiCoO}_2$  ( $\text{Co}^{3+}$ ), and  $\text{Sr}_6\text{Co}_5\text{O}_{15}$  ( $\text{Co}^{3.6+}$ ). The baseline of the reference spectra are offset to a higher absorbance for clarity. (d) The corresponding NMF derived spectra from the cluster averaged circled regions in (b). In (c,d) the reference spectra have been offset from the PCA and NMF end member spectra. End members 1 and 2 for both the PCA and NMF analysis closely match the reference compound spectra for  $\beta\text{-Co(OH)}_2$  and  $\text{LiCoO}_2$  while end member 3 corresponds to noise from the background absorption by the electrolyte/electrode substrate. We note that the PCA/NMF analysis did not yield any spectra with an apparent Co oxidation state over  $3+$ .

significant redundancy with each other and for the most part only explain changes in a very limited energy range. Likely this is a result of the high degree of background absorption through the relatively thick electrolyte and small changes in path length through the electrolyte across individual images which yield large changes in absorbance due to the short absorption length of the soft x-rays. Notably, none of the first 5 principal components contain a peak at 782 eV which would be expected for  $\text{Co}^{4+}$  species. We conclude that the remaining variance beyond 77% is mostly noise and that the data can adequately be described by the first two principal components, thereby reducing the dimensionality of the data from  $[x, y, 118]$  to  $[x, y, 2]$ . However, to ensure that we are not ignoring contributions from other influential components, we include three components in our analysis described below. Still, as will be clear, only two components are needed to describe the full data set.

Once we have identified the principal components, we project the data into 3-dimensional PCA space to identify the extreme points (end member spectra), as shown in Figure S6a. We average a small cluster of the observed single pixel spectra at the extremes that bound the data in PCA space to find the true end member spectra. We also perform the same analysis with non-negative matrix factorization (NMF) as shown in Figure S6b. We view the NMF analysis as a more valid approximation of the end member spectroscopy as it is constrained to non-negative combinations of non-negative components, thus more closely resembling the real spectral components. This is clear in Figure S6c and Figure S6d which correspond to the end members

derived through PCA and NMF analysis, respectively, where the end members 1 and 2 have negative contributions at energies  $< 776.5$  eV in the PCA spectra but positive in the NMF spectra. Regardless, both analysis methods yield similar results for all three end member spectra, with PCA/NMF end member 1 spectra closely resembling the spectra of a pristine  $\beta$ -Co(OH)<sub>2</sub> reference spectra (corresponding to Co<sup>2+</sup>) and PCA/NMF end member 2 spectra closely resembling the spectra of a LiCoO<sub>2</sub> reference spectra (corresponding to Co<sup>3+</sup>). It should be noted that there is a weighting of intensity at the high energy shoulder in the LiCoO<sub>2</sub> spectra which is likely due to a small degree of lithium vacancies in the compound, corresponding to a cobalt oxidation state slightly higher than 3+. As noted above, the third end member component for both PCA and NMF does not correspond to a cobalt containing species but instead is a signature of the background absorbance by the electrolyte which increases linearly with increasing X-ray photon energy. The high absorbance of this end member is an artifact of the normalization procedure. As such, we discard the third end member in our further analysis. We include a reference compound containing 60% Co<sup>4+</sup>, Sr<sub>6</sub>Co<sub>5</sub>O<sub>15</sub>, as a comparison demonstrating that the PCA and NMF end member 2 does not contain Co<sup>4+</sup> contributions.

Although PCA/NMF end member 2 is very similar in position and intensity to the LiCoO<sub>2</sub> reference, there have been a number of studies that suggest Co<sup>4+</sup> should exist at high voltages when the OER is occurring. As such, instead of assuming that end member 2 corresponds to Co<sup>3+</sup>, we analyze the oxidation state of this spectra using an ideal solution model, as described below. As mentioned previously, we opt for using the NMF-cluster-spectra rather than PCA as they are more representative of the real spectroscopic signatures. To perform the ideal solution model fitting analysis, the average spectra for a particle at a given voltage is first obtained, shown in Figure S7a. End Member 1 is assigned an oxidation state of 2+ while End Member 2 is assigned an oxidation state of  $(2+n_1+n_2)+$  due to the two redox reactions observed during cyclic voltammetry. The spectra are first fit with a linear combination of the end member spectra and plotted as the percent of End Member 2 versus voltage, as shown in Figure S5b, where the error bars correspond to the standard deviation of End Member 2 percent for fits of the single pixel spectra. An ideal solution model, corresponding to Nernstian electrochemical behavior, is derived, where  $n_1$  corresponds to the number of electrons transferred during the first redox reaction with a reversible voltage  $E_1^{0'}$ ,  $n_2$  corresponds to the number of electrons transferred during the second redox reaction with reversible voltage  $E_2^{0'}$ , and  $E$  corresponds to the voltage at which the spectro-image was acquired. The fraction of each phase is described through the term  $[Co^i]$  (where  $i$  is the oxidation state of the pure phase) and conservation of mass is ensured through Equation (S3). We note that the spectra for the intermediate phase at voltages between 1.3 - 1.5 V vs. RHE, corresponding to an oxidation state of  $(2+n_1)+$ , is a mixture of the open circuit voltage End Member 1 phase (Co<sup>2+</sup>) and the high voltage End Member 2 phase.

$$\frac{[Co^{(2+n_1)+}]}{[Co^{2+}]} = e^{f[n_1(E-E_1^{0'})]} \quad (S3)$$

$$\frac{[Co^{(2+n_1+n_2)+}]}{[Co^{(2+n_1)+}]} = e^{f[n_2(E-E_2^{0'})]} \quad (S4)$$

$$[Co^{2+}] + [Co^{(2+n_1)+}] + [Co^{(2+n_1+n_2)+}] = 1 \quad (S5)$$

The average oxidation state derived through the ideal solution model is thus:

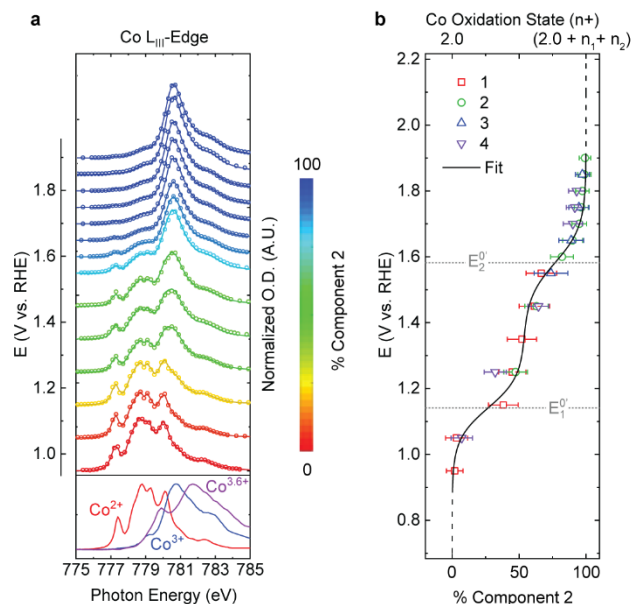


**Figure S7 | Solid state ideal solution fit of end member oxidation states.** (a) Average voltage dependent single particle Co  $L_{III}$  edge XAS spectra (points) color mapped according to a linear combination of NMF derived Component 1 and Component 2 end member spectra (points are experimental data, lines represent the fit). The spectra are offset on the y-axis such that the intercept at 775 eV corresponds to the steady state voltage at which they were acquired. (b) Percent NMF Component 2 (versus Component 1) versus voltage. The data was fit assuming two separate redox reactions according to the cyclic voltammetry data with Component 1 having an oxidation state of  $2+$ . Error bars represent the single standard deviation of a normal distribution fit of the single pixel XAS spectra from the STXM spectro-images.

$$n +_{model} = 2[Co^{2+}] + (2 + n_1)[Co^{(2+n_1)+}] + (2 + n_1 + n_2)[Co^{(2+n_1+n_2)+}] \quad (S6)$$

and the corresponding STXM-XAS oxidation state is:

$$n +_{STXM} = 2 + (2 + n_1 + n_2)[EndMember2] \quad (S7)$$

The experimental STXM-XAS data is fit to the model by minimizing the root mean square error ( $R$ ) where  $\nu$  is the degrees of freedom in the fit:

$$R = \left( \frac{1}{\nu} \sum (n +_{model} - n +_{STXM})^2 \right)^{0.5} \quad (S8)$$

From the fit, it was determined that the first redox reaction corresponds to the transfer of  $n_1 = 0.54 \pm 0.04$  electrons at  $E_1^{0'} = 1.14 \pm 0.03$  V vs. RHE and the second redox reaction corresponds to the transfer of  $n_2 = 0.46 \pm 0.04$  electrons at  $E_2^{0'} = 1.58 \pm 0.03$  V vs. RHE with an RMS error of  $R = 0.254$  thus confirming that End Member 2 does indeed correspond to the spectra of  $Co^{3+}$ . The derived reversible voltages from the ideal solution model show excellent agreement with the position of the observed redox peaks in the cyclic voltammograms shown in the main text Figure 1d and 4d. The error in the derived number of electrons transferred and reversible voltages is the 95% confidence interval and is calculated as follows.

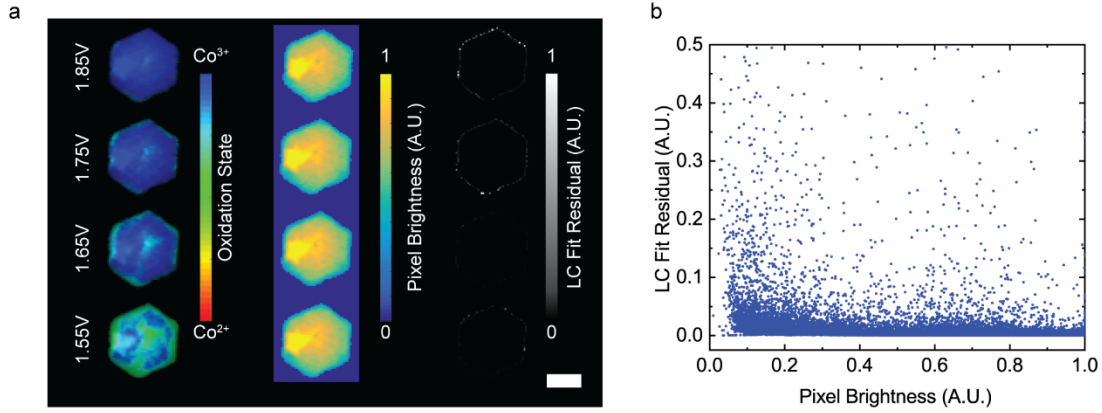


**Figure S8 | Linear combination fitting analysis** (a) Phasemaps (left), particle thickness/brightness (center), and greyscale residual maps (right) for the particles at OER voltages. (b) Plot of the single pixel linear combination fit residual versus the pixel brightness for the complete dataset. The brightness is linearly proportional to the integrated Co  $L_{III}$ -edge area of the single pixel spectrum. In general, the residuals are below 0.05 except for some pixels at the edges of the particles. The higher edge residuals may be a result of subpixel offsets in the image stack alignment and the lower particle thickness which results in less bright pixels for the fitting. It should be noted that the higher residual is limited to a thickness of one single pixel at the edge of the particles.

$E_1^{0'}$ ,  $E_2^{0'}$ ,  $n_1$ , and  $n_2$  are the four fitting parameters and are fit to 26 data points yielding a degree of freedom ( $\nu$ ) of 22. The 95% confidence interval (CI) is calculated as, where  $t$  is the value of the student's t-distribution with  $\nu = 22$  and  $\alpha = 0.025$ , and  $\text{diag}$  is an operator that takes the diagonal of the matrix  $\sqrt{S}$ :

$$CI = \pm t_{\alpha=0.025, \nu=22} \text{diag}(\sqrt{S}) \quad (S9)$$

The covariance matrix,  $S$ , is defined as:

$$S = R^2(A^T A)^{-1} \quad (S10)$$

Where  $A$  is the Jacobian matrix of the fitted values with regards to the fitted coefficients,  $A^T$  is the transpose matrix of  $A$ , and  $R^2$  is the mean square error:

$$R^2 = \frac{1}{\nu} \sum (n_{+model} - n_{+STXM})^2 \quad (S11)$$

The Jacobian matrix  $A$  is the partial derivative matrix of  $n_{+model}$  with respect to the fitting parameters, i.e.:

$$A = \begin{bmatrix} \frac{\partial n_{+model,1}}{\partial E_1^0} & \frac{\partial n_{+model,1}}{\partial E_2^0} & \frac{\partial n_{+model,1}}{\partial n_1} & \frac{\partial n_{+model,1}}{\partial n_2} \\ \frac{\partial n_{+model,2}}{\partial E_1^0} & \frac{\partial n_{+model,2}}{\partial E_2^0} & \frac{\partial n_{+model,2}}{\partial n_1} & \frac{\partial n_{+model,2}}{\partial n_2} \\ \vdots & \vdots & \vdots & \vdots \\ \frac{\partial n_{+model,26}}{\partial E_1^0} & \frac{\partial n_{+model,26}}{\partial E_2^0} & \frac{\partial n_{+model,26}}{\partial n_1} & \frac{\partial n_{+model,26}}{\partial n_2} \end{bmatrix} \quad (S12)$$

Having confirmed that End Member 1 corresponds to  $\text{Co}^{2+}$  and End Member 2 corresponds to  $\text{Co}^{3+}$ , we then perform a non-negative linear least squares regression on every

normalized pixel to calculate the fraction of each end member present. The quality and goodness of fit for the linear combination (LC) of NMF End Members 1 and 2 were evaluated by spatially mapping the residuals of the fit. Figure S8a shows the residuals for the phase map data taken in the OER potential region ( $E > 1.55$  V vs. RHE) demonstrating great fidelity in fit with residuals slightly increasing in the single pixel region at the edges of the particles. Outside of this single pixel edge region, there are no domains with high residuals. We attribute the higher residuals at the edge to be from sub-pixel misalignment in the image stacks that cause noise in the single pixel spectra. Most pixels have residuals  $< 0.05$ , as shown in Figure S8b, which is less than 5% of the 2-norm of the NMF end members. Most pixels with higher residuals have a brightness below 0.1 and as such do not significantly influence the analysis.

Once the fractions of the End Member components are calculated at each pixel, a color on the HSV color scale is assigned corresponding to the fraction of End Member 2, such that 0% has a hue of 0 (red) and 100% has a hue of  $2/3$  (blue). Saturation is uniformly set to 100% and the brightness of each pixel is set to be linearly proportional to the integrated Co L<sub>III</sub>-edge area, yielding the presented spectro-images. These spectro-images yield important information about the distributions in oxidation state at the subparticle level that is not achievable (and thus overlooked) in standard hard and soft x-ray spectroscopy approaches.

#### *UV-Vis Spectroelectrochemistry:*

Spectroelectrochemistry was performed using a commercial flow cell (SEC-2F, BAS Inc.) coupled to a Xenon light source (HAL-320, Asahi Spectra), monochromator (CMS-100, Asahi Spectra) and spectrometer (B2000+, Ocean Optics) through fiber optic cables. The electrode was a  $200 \mu\text{g cm}^{-2}_{\text{geom}}$  dropcast thin film of  $\beta\text{-Co(OH)}_2$  with 1 wt% Na-substituted Nafion on indium-tin oxide (ITO) coated glass. Prior to dropcasting  $\beta\text{-Co(OH)}_2$ , the ITO glass was cleaned through sonication with ethanol, followed by acetone, followed by ethanol, followed by DI water through sonication for 5 minutes each. The ITO glass electrodes were then  $\text{O}_2$  plasma cleaned for 3 minutes. Spectra were acquired with a 35 ms dwell time and averaged over 1200 scans. Electrochemistry was performed at constant voltage in 50 mV increments from 0 - 0.95 V vs. Ag/AgCl holding for 2 h at each voltage. The spectra reported correspond to the last spectra at a given voltage corresponding to the steady state absorbance of the  $\text{CoO}_x\text{H}_y$  material.

#### *Powder X-ray Diffraction:*

Samples were prepared at a mass loading of  $50 \mu\text{g cm}^{-2}_{\text{geom}}$  of  $\beta\text{-Co(OH)}_2$  on  $1 \times 1 \text{ cm}^2$  ITO coated glass (MSE Supplies) and chronoamperometry was performed in 0.1 M KOH at the indicated voltages in Figure S12 for 24 hours. The electrodes were then gently washed with DI water and allowed to dry naturally at room temperature. Post-mortem powder X-ray diffraction was performed using a Bruker D8 Advance Diffractometer with Cu K- $\alpha$  ( $\lambda = 1.5406 \text{ \AA}$ ) radiation between  $2\theta = 10 - 90^\circ$ , an acquisition time of 15 minutes, and a step size of  $2\theta = 0.02^\circ$ .

## Supplementary Discussion:

### *Is Co<sup>4+</sup> Present during the OER in the CoO<sub>x</sub>H<sub>y</sub> System?*

CoO<sub>x</sub>H<sub>y</sub> is an archetypal member of the family of transition metal (oxy)hydroxide electrocatalysts.<sup>5,6,12,26,48,49</sup> Tabulated Co-H<sub>2</sub>O equilibria in alkaline electrolytes ( $pH > \sim 8.5$ ) suggests the bulk phase stability to proceed from Co to Co(OH)<sub>2</sub> ( $E^{0'} = 0.08$  V vs. RHE) through the spinel Co<sub>3</sub>O<sub>4</sub> ( $E^{0'} = 0.577$  V vs. RHE) to the layered CoOOH ( $E^{0'} = 1.15$  V vs. RHE) and then to the layered CoO<sub>2</sub> ( $E^{0'} = 1.76$  V vs. RHE) structures as the voltage is increased anodically through the OER regime.<sup>12,50</sup> However, it has been noted that the thermodynamic data for the higher oxides (specifically CoOOH and CoO<sub>2</sub>) may not be reliable<sup>51</sup> and there are also proposed metastable CoO<sub>x</sub>H<sub>y</sub> phases with variable proton content, interlayer water, and/or charge balancing ions.<sup>28,29,52,53</sup>

Complicating the matter, a number of fundamental studies on CoO<sub>x</sub>H<sub>y</sub> OER catalysts (i.e. “Co-Pi”<sup>54</sup>) use electrodeposited electrodes with low crystallinity as model systems.<sup>8,26,28,52,54–56</sup> Because of this, the active structure and Co oxidation state during the OER remains inconclusive.<sup>26,27,48,57–61</sup> Still, regardless of the initial phase of the oxide or its crystallinity, the OER is observed at voltages anodic of  $\sim 1.55$  V vs. RHE for the CoO<sub>x</sub>H<sub>y</sub> (oxy)hydroxide system, demonstrating a common active site required to turnover O<sub>2</sub>.<sup>26,30,48,57,62–64</sup> While some recent bulk-sensitive *operando* experiments using Co K-edge X-ray absorption near edge structure (XANES) and extended X-ray absorption fine structure (EXAFS) suggest CoOOH<sub>y</sub>-like molecular motifs with  $y < 1$  and an active state of Co<sup>4+</sup> to prevail during the OER<sup>28,29,52</sup>, other similar experiments find the conversion of Co<sub>3</sub>O<sub>4</sub> to CoOOH with Co<sup>3+</sup> to initiate the OER<sup>65</sup>. Surface sensitive experiments including ambient pressure X-ray photoelectron spectroscopy (AP-XPS)<sup>61,66</sup> and surface X-ray diffraction measurements<sup>62,66–68</sup> have not resolved this debate; the results suggest a CoOOH-like structure but differ over whether or not Co<sup>4+</sup> is present during the OER.

The suggestion of Co<sup>4+</sup> in the CoO<sub>x</sub>H<sub>y</sub> system was first proposed through ex-situ electron paramagnetic resonance (EPR) measurements on Co-Pi (CoCat) samples frozen during active water electrolysis. In this original work, a signal at  $g_{eff} = 2.27$  was assigned to Co<sup>4+</sup> and proposed to be the active site for the OER.<sup>27</sup> Yet, later work comparing Co-Pi to Co<sup>4+</sup> containing molecular analogs with higher resolution ENDOR spectroscopy could not confirm this earlier assignment.<sup>69</sup> Further, more extended voltage dependent<sup>26</sup> and *operando*<sup>70</sup> EPR data on the Co-Pi system demonstrated that the  $g_{eff} \sim 2.2$  signal disappears during the OER, and therefore represents a pre-catalytic state. While a signal corresponding to tetrahedrally coordinated Co<sup>2+</sup> was discarded in the original work<sup>27</sup> by comparing to a Co<sub>3</sub>O<sub>4</sub> standard spectrum, this spectrum differs significantly from other reported Co<sub>3</sub>O<sub>4</sub> EPR spectra, where  $g_{eff}$  values between 2.17–2.30 are generally observed.<sup>71–74</sup> Importantly, these  $g$ -values are in agreement with tetrahedral Co<sup>2+</sup> containing molecular analogs.<sup>75</sup> Additionally, nearly identical spectra to Co-Pi are obtained for “ $\alpha$ -Co(OH)<sub>2</sub>” which has an average Co oxidation state near 2.5+, tetrahedrally coordinated Co<sup>2+</sup>, and the presence of interlayer water.<sup>76–78</sup> The attributes of the  $\alpha$ -Co(OH)<sub>2</sub> phase agree well with our results on the intermediate voltage phase of the  $\beta$ -Co(OH)<sub>2</sub> particles. We emphasize that tetrahedrally coordinated Co<sup>2+</sup> provides an alternative and more general explanation for the increased intensity in the pre-edge feature observed in previous Co K-edge measurements on CoO<sub>x</sub>H<sub>y</sub> systems.<sup>52</sup>

While our results do not show evidence of  $\text{Co}^{4+}$  formation during the OER, we cannot absolutely exclude its presence as a reaction intermediate. Indeed, if the rate of  $\text{O}_2$  generation from the  $\text{Co}^{4+}$  state is much faster than the generation of  $\text{Co}^{4+}$  from  $\text{Co}^{3+}$ , then our steady state STXM-XAS measurements may not capture the  $\text{Co}^{4+}$  formation. However, as previously determined through our microkinetic modeling, the OER Tafel behavior of this system is related to the surface concentration of the active site, which we find to be  $\text{Co}^{3+}$  in  $\beta\text{-CoOOH}$ .<sup>5</sup> The OER on this phase is limited by the conversion  $\text{OH}^* \rightarrow \text{O}^*$  with an intrinsic turnover rate of  $k^0 = 1700 \text{ s}^{-1}$  per Co site.<sup>5</sup> While the  $\text{O}^*$  intermediate is generally formulated as  $\text{Co}^{4+}=\text{O}^{2-}$ ,<sup>60,79</sup> Bader charge analysis of the reactant and product states of the RLS suggest no change in electron density surrounding Co and the formation of an oxidized  $\text{Co}^{3+}-\text{O}^{1-}$  surface as the product of the RLS, which agrees with the absence of a detectable  $\text{Co}^{4+}$  signal in our measurements.<sup>5</sup>

Assuming that high valent redox is a requirement for the OER, the absence of observable  $\text{Co}^{4+}$  reflects how the extended coordination of the  $\text{CoO}_x$  structure controls the production of  $\text{Co}^{3+/4+}$  and  $\text{O}^{2-/1-}$ . In structures with face-sharing  $\text{CoO}_6$  octahedra (i.e.  $\text{Sr}_6\text{Co}_5\text{O}_{15}$ , Figure 4b) reduced hybridization between Co and O expands the charge-transfer gap allowing for cationic redox and formation of  $\text{Co}^{4+}$ .<sup>80</sup> However, this structure, with associated  $\text{Co}^{4+}$ , is less active<sup>81</sup> but more stable than high-valent structures with corner-sharing  $\text{CoO}_6$  (i.e.  $\text{SrCoO}_{3-\delta}$ ),<sup>82</sup> which preferentially form oxidized lattice oxygen with associated  $\text{Co}^{3+}$ , rather than  $\text{Co}^{4+}$ , due to increased Co-O hybridization. The Co (oxy)hydroxide system, with edge-sharing  $\text{CoO}_6$  octahedra thus represents an intermediate structure with high stability but activity limited by the barriers to form either  $\text{Co}^{4+}$  or  $\text{O}^{1-}$ .<sup>6</sup>

#### *Co L-edge versus K-edge XAS for Oxidation State Assignment:*

Our STXM approach quantifies oxidation state through Co L<sub>III</sub>-edge measurements, which directly probe the electron population of the redox active Co 3d states ( $\text{Co } 2p \rightarrow 3d$  transitions). These L-edge spectra serve as “fingerprints” of the oxidation state and coordination environment around Co and can be easily identified by linear combinations of standard spectra (Main Text Figure 4b). In comparison, more commonly used K-edge measurements<sup>8,28,29,52</sup> probe  $1s \rightarrow 4p$  or continuum states, where oxidation state assignment occurs through the determination of the “edge position”. However, the shape of the edge, and thus the extraction of position, is often complicated by local coordination and extended structure, ligand-to-metal charge transfer, and core hole effects.<sup>83</sup> Indeed, the edge shape and position has wide variability for Co oxides, even with nominally the same oxidation state and coordination environment.<sup>28,84</sup> Lastly, the direct absorbance measurements performed in STXM do not suffer from the self-absorbance effects that influence the spectroscopy using the fluorescent yield detection common in general Co L- and K-edge approaches.<sup>85,86</sup>

#### *UV-Vis Spectroelectrochemistry:*

It is well known that  $\text{CoO}_x\text{H}_y$ 's are electrochromic materials that change their optical properties from a pink colored brucite type  $\beta\text{-Co(OH)}_2$  to a dark brown/black colored  $\beta\text{-CoOOH}$  with increasing voltage and Co oxidation state.<sup>28,53,87,88</sup> We perform steady state UV-Vis spectroelectrochemistry, shown in Figure S9, as a means of comparing our single-particle results to ensemble average measurements of the  $\text{CoO}_x\text{H}_y$  system previously reported.<sup>28</sup> A thin film of  $\beta\text{-Co(OH)}_2$  on indium-tin oxide (ITO) coated glass was charged at increasing constant applied voltages and the optical absorbance spectrum was recorded under steady state conditions

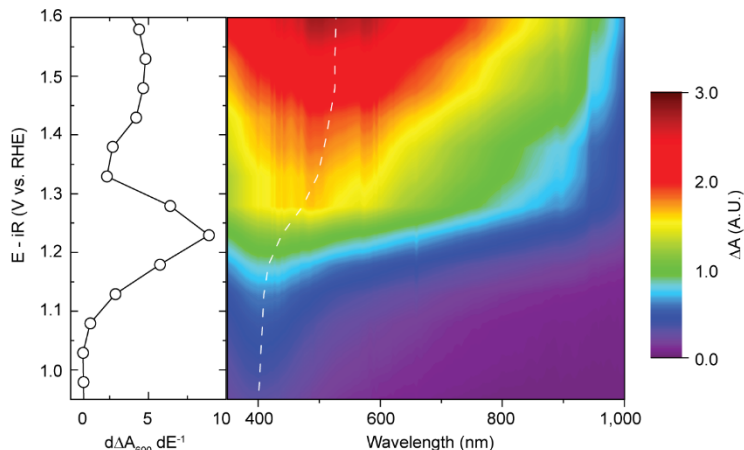


**Figure S9 | Ensemble UV-Vis spectroelectrochemistry of  $\beta$ -Co(OH) $_2$  platelet particles in 0.1 M KOH.** Steady-state voltage dependent operando UV-Vis spectroelectrochemistry normalized by the initial  $\beta$ -Co(OH) $_2$  adsorption at OCV ( $E = 0.95$  V). Data points represent the final absorbance after holding at the indicated voltage for 2 hours. The center of gravity for the absorbance peak is indicated with the dashed white line which shows the transition from the pink brucite  $\beta$ -Co(OH) $_2$  through two additional phases associated with absorption centers of gravity at  $\sim 400$  nm and  $520$  nm. The derivative of the absorbance with respect to voltage is shown below and indicates two transitions that agree well with the redox peaks observed electrochemically.

(after 2 hours at a given voltage) and plotted normalized by the initial open-circuit  $\beta$ -Co(OH) $_2$  absorbance. With increasing voltage there is an increase in the absorbance at a center of gravity of  $402$  nm followed by a transition to longer wavelength and increased absorbance at  $528$  nm, suggesting oxidation of the Co atoms and decreasing bandgap. The derivative of the absorbance at  $600$  nm indicates two redox transitions with half wave potentials of  $\sim 1.2$  and  $\sim 1.55$  V vs. RHE which correspond well with the previously observed redox peaks for the particles. These results also correspond well with previous UV-Vis spectroelectrochemistry on electrodeposited films of amorphous hydrated  $\text{CoO}_x\text{H}_y$  containing structural cations and anions from the deposition electrolyte (“CoPi” or “CoCat”) by Risch *et al.* that demonstrated an absorbance maximum at  $405$  nm for a film with a proposed nominal Co oxidation state of  $\sim 2.6+$  after deposition increasing to  $515$  nm with increasing voltage corresponding to a film with a proposed nominal Co oxidation state of  $\sim 3.25+$ .<sup>27–29,54</sup> Despite differences in the extended crystallinity of the as deposited materials, the similarities in the operando optical absorbance suggest similar intermediate compositions and Co oxidation states among the  $\text{CoO}_x\text{H}_y$  family.

#### Window Bowing:

The interior of the flow cell, inside the flow channel between the sandwiched spacer and electrode chips, is at atmospheric pressure while the environment outside of the cell in the microscope is generally filled with 200 torr of He gas. This pressure differential causes the  $\text{SiN}_x$  windows to bow resulting in a varying X-ray path length across the width of the window. In the single pixel ( $50$  nm) limit, this effect is not noticeable, but over the full image size (which may be on the order of  $6 \times 6$   $\mu\text{m}$ ) this may cause a variation in absorbance that has to be accounted for. Due to the number of transmitted photons exponentially decreasing with path length according to the Beer-Lambert law, the bowing of the electrolyte can be calculated according to the following series of equations, where  $I$  is the number of transmitted photons at a given X-ray energy,  $I_0$  is the incident flux of photons at a given X-ray energy,  $\mu$  is the mass absorption

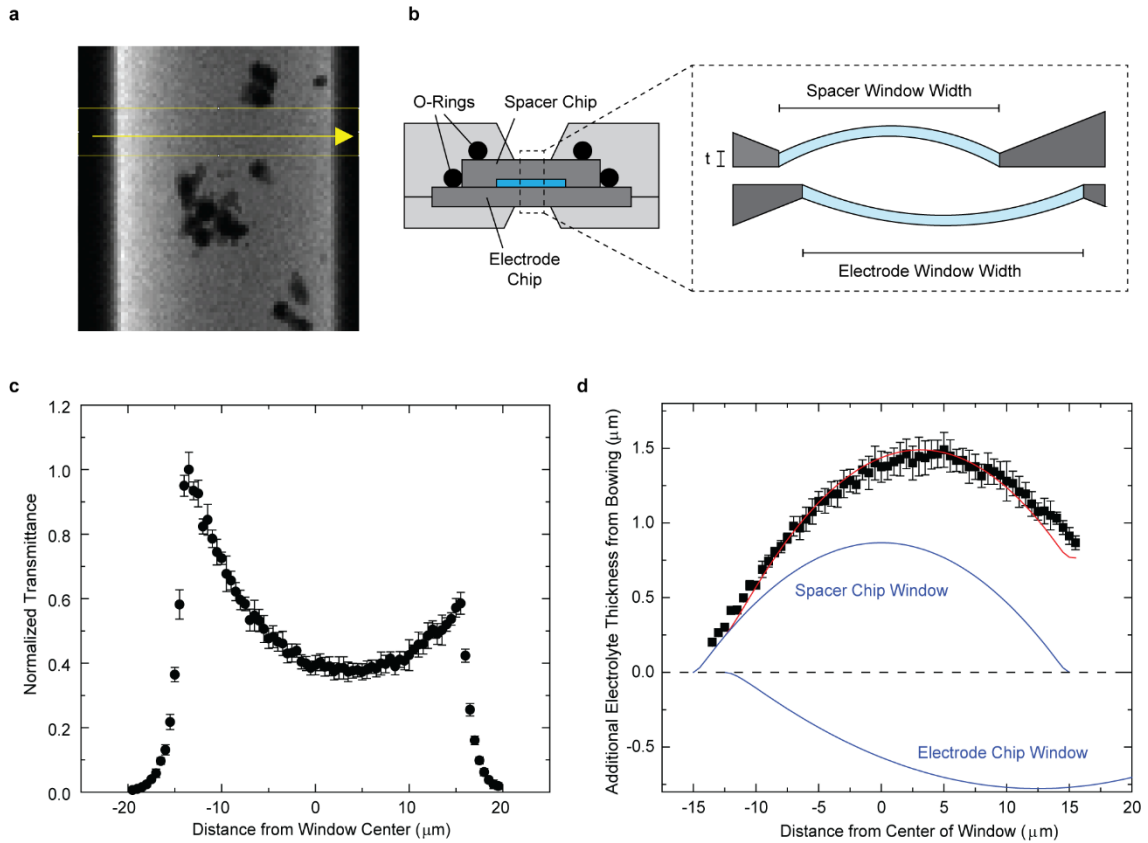


**Figure S10 |  $\text{SiN}_x$  Window Bowing Analysis.** (a) Image of the window taken at 778.5 eV. (b) Side view of the sandwich chip design and flow channel. Enlarged section shows a depiction of the window bowing for chips with slight offset windows. The spacer chip window width and the electrode chip window width were  $30\ \mu\text{m}$  and  $50\ \mu\text{m}$  in this example. (c) Normalized photon transmittance for the line scan shown in yellow in (a). (d) Analysis showing bowing of each window on the order of  $750\ \text{nm}$  at the mid-point.

coefficient at a given X-ray energy,  $\rho$  is the density of the species through which the X-ray is passing,  $x$  is the path length,  $t$  is the thickness of the  $\text{SiN}_x$  window ( $100\ \text{nm}$  for each window),  $E$  is Young's Modulus ( $95\ \text{GPa}$  for  $\text{SiN}_x$ ), and  $s$  is the built-in stress ( $250\ \text{MPa}$  for  $\text{SiN}_x$ ). The results are presented in Figure S10, where a bowing of each window on the order of  $750\ \text{nm}$  was calculated. Note that there was a slight offset of the windows such that their centers were not aligned, but this was accounted for in the calculation.

$$I = I_0 e^{-\mu\rho x} \quad (\text{S13})$$

$$D \frac{d^4}{dx^4} d(x) - ts \frac{d^2}{dx^2} d(x) = P \quad (\text{S14})$$

$$E_{ps} = \frac{E}{1-\nu^2} \quad (\text{S15})$$

$$D = \frac{E_{ps} t^3}{12} \quad (\text{S16})$$

## Radiation Effects:

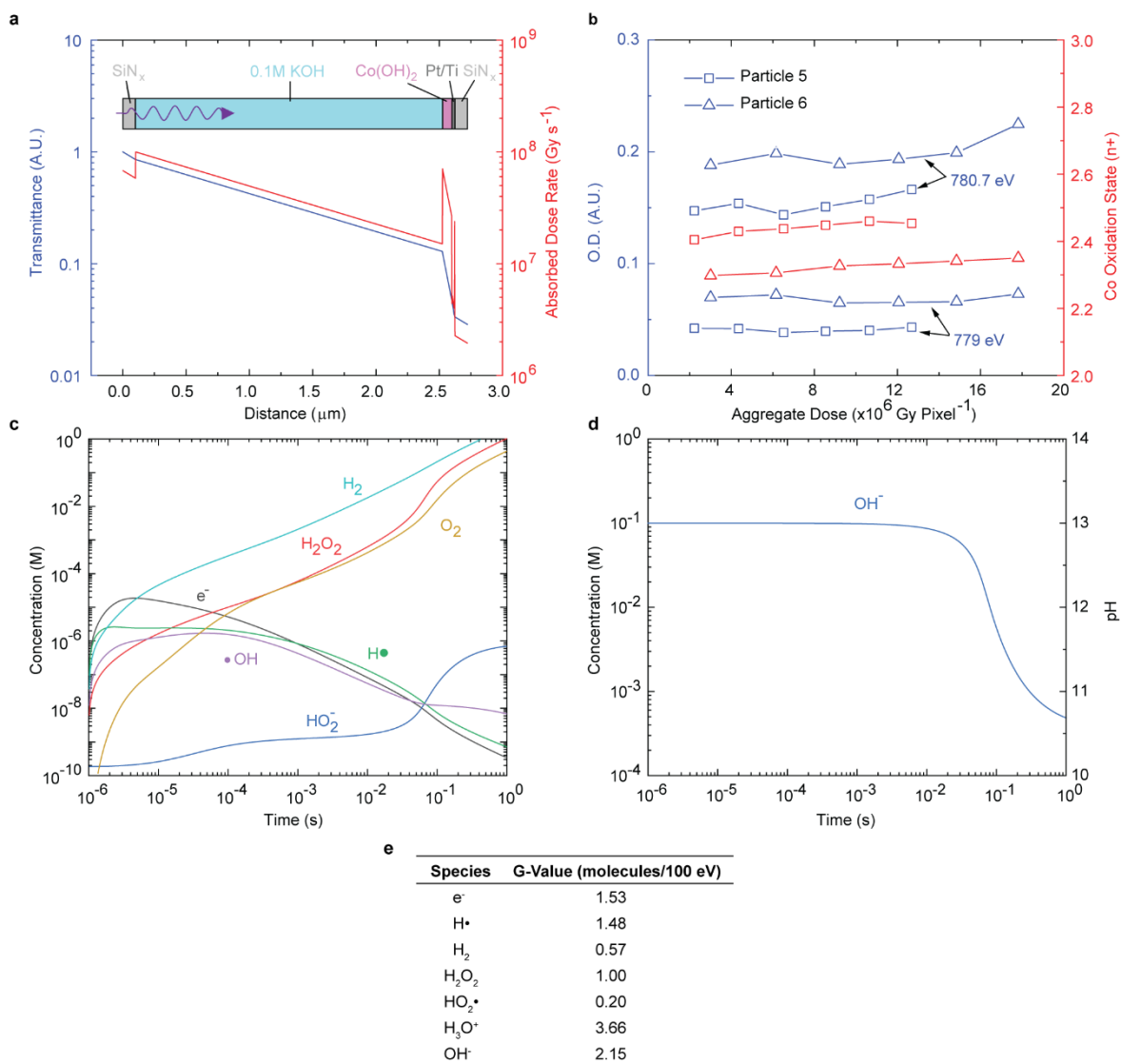


**Figure S11 | Effects of X-ray Radiation on Particle and Electrolyte.**<sup>90</sup> (a) Transmittance and radiation dose rate through the thickest part of the cell, assuming a 100 nm  $\text{SiN}_x$  window, 2.425  $\mu\text{m}$  thick 0.1 M KOH electrolyte, 75 nm thick  $\text{Co(OH)}_2$ , and 20/5 nm Pt/Ti electrode. The direction of the photon path is shown in the Figure. (b) Stability of the sample under the X-ray beam. Even for high aggregate X-ray doses per pixel there is no observed photoreduction. (c) Primary radiolysis product yields from the electrolyte versus time and (d) Hydroxide ion concentration and pH versus time for a dose rate of  $4.5 \times 10^7 \text{ Gy s}^{-1}$  at 780 eV. Note that the x-ray dwell time is 2 ms  $\text{pixel}^{-1}$  where the majority of radiolysis products are at sub mM concentrations. In addition, there is a 2 ms delay between pixel acquisitions. With a flow rate of electrolyte through the cell is  $30 \mu\text{L min}^{-1}$ , the electrolyte inside the cell is replaced every 3 ms meaning that each pixel acquisition is in fresh electrolyte. (e) Table of G-Values for 780 eV electrons in liquid water from Hill and Smith.<sup>91</sup>

The flux at Beamline 11.0.2.2 at the Advanced Light Source at Lawrence Berkeley National Lab is on the order of  $3 \times 10^7 \text{ photons s}^{-1}$ . Zone plates have a first order diffraction efficiency on the order of 10% yielding a photon flux of  $\sim 3 \times 10^6 \text{ photons s}^{-1}$  incident on the sample. The transmittance ( $T = I/I_0$ ) of the cell can be modeled using Equation S13 allowing for

the calculation of the absorbed radiation dose rate, as shown in Figure S11a. The system was modeled at an X-ray energy of 778.7 eV, corresponding to the most intense absorption peak in to Co L<sub>III</sub>-edge spectrum of  $\beta$ -Co(OH)<sub>2</sub>. Assuming an absorbance of 1, this corresponds to a mass extinction coefficient for  $\beta$ -Co(OH)<sub>2</sub> of  $\mu_{778.7}^{Co(OH)_2} = 37037 \text{ g}^{-1} \text{ cm}^{-2}$ . Other constants used in the calculation are:  $\rho_{Co(OH)_2} = 3.6 \text{ g cm}^{-3}$ ,  $\rho_{SiN_x} = 3.44 \text{ g cm}^{-3}$ ,  $\rho_{Pt} = 21.44 \text{ g cm}^{-3}$ ,  $\rho_{Ti} = 4.54 \text{ g cm}^{-3}$ ,  $\rho_{0.1 \text{ M KOH}} = 1 \text{ g cm}^{-3}$ ,  $\mu_{778.7}^{SiN_x} = 4542 \text{ g}^{-1} \text{ cm}^{-2}$ ,  $\mu_{778.7}^{Pt} = 7531 \text{ g}^{-1} \text{ cm}^{-2}$ ,  $\mu_{778.7}^{Ti} = 10584 \text{ g}^{-1} \text{ cm}^{-2}$ ,  $\mu_{778.7}^{0.1 \text{ M KOH}} = 7813 \text{ g}^{-1} \text{ cm}^{-2}$ .<sup>89</sup> A pixel size of 50x50 nm was used with 100 nm SiN<sub>x</sub> windows, 2.425  $\mu\text{m}$  thick 0.1 M KOH electrolyte, 75 nm thick Co(OH)<sub>2</sub>, and a 20 nm/2 nm thick Pt/Ti electrode coating. Using a dwell time of 2 ms per energy per pixel, the 0.1 M KOH electrolyte and the  $\beta$ -Co(OH)<sub>2</sub> particles experience dose rates of the order of  $10^7 \text{ Gy s}^{-1}$ . Note that imaging in water in a liquid cell using Scanning Transmission Electron Microscopy (STEM) at 30 keV and a beam current at 0.05 nA focused to the same spot size (beam radius = 25 nm), which are mild conditions for STEM imaging, has a dose rate of  $2.5 \times 10^{10} \text{ Gy s}^{-1}$ . This dose rate is  $\sim 3$  orders of magnitude higher than the dose rates used in this study.<sup>46</sup> Imaging using fluorescence yield (FY) and hard X-rays with Transmission X-ray Microscopy ( $E > 1000 \text{ eV}$ , TXM) similarly has dose rates  $\sim 3$  orders of magnitude higher than the STXM experiments.

X-ray radiation has previously been shown to photo-reduce particles with high oxidation state due to the generation of high energy electrons. To investigate this effect on our samples, the oxidation state of two particles was measured over repetitive imaging conditions, in which the aggregate dose increased from  $3 \times 10^6$  to  $18 \times 10^6 \text{ Gy pixel}^{-1}$ , as shown in Figure S11b. Although there is variation in the relative optical density (O.D.) between successive imaging, the measured oxidation state for both particles was not found to decrease over time. At the highest aggregate dosage, there was no observed photoreduction.

To better understand this effect, we model the primary product yields for the radiolysis of the electrolyte at 780 eV using the model developed by *Schneider et al.* as shown in Figure S11c,d.<sup>90</sup> G-values at 780 eV were interpolated from data found in Hill and Smith and are shown in Figure S11e.<sup>91</sup> Note that the G-Value in Table 1 for H<sub>2</sub> is likely higher than the true value and was found by carrying out atomic balances for both the hydrogen and oxygen atoms produced from water destruction (inspection of the data in Hill and Smith suggests it is close to 0).<sup>91</sup> At soft x-ray energies ( $E < 1000 \text{ eV}$ ), the primary effect of X-rays interacting with matter is the ejection of electrons from the material,<sup>92,93</sup> and as such modeling the radiolysis products as being derived from electrons with the X-ray photon energy is valid.

During the X-ray dwell time at each pixel, 2 ms, the major products produced are O<sub>2</sub>, H<sub>2</sub>O<sub>2</sub>, and H<sub>2</sub>, although the H<sub>2</sub> yield may be artificially inflated as stated above. All of the products are below mM concentrations, with the majority at sub  $\mu\text{M}$  concentrations, and there is no change in the electrolyte hydroxide concentration. In addition, many of these products are speculated as intermediates in the OER ( $\bullet\text{OH}$ , HO<sub>2</sub> $\bullet$ , and O<sub>2</sub>). With high oxidation strength (low standard reduction potentials) and low concentrations, this may explain why we do not see significant photoreduction effects. However, as the  $\bullet\text{OH}$  and HO<sub>2</sub> $\bullet$  radicals are associated with Co<sup>3+</sup>, the radiolysis effects may prevent observation of Co<sup>4+</sup> if it existed at the surface of the particles as has been previously speculated. Regardless, we use a 2 ms delay between acquisition of subsequent pixels. With a flow rate of electrolyte of  $30 \mu\text{L min}^{-1}$ , the electrolyte inside the cell is replaced every 3 ms and each pixel acquisition is taken in fresh electrolyte. We believe that the

rate of electrolyte replenishment is sufficient to maintain the true oxidation state of the particles during STXM imaging with minimal photoreduction.

*Ex-situ STXM and XRD analysis of relaxed  $\beta$ -Co(OH)<sub>2</sub> particles after oxidation:*

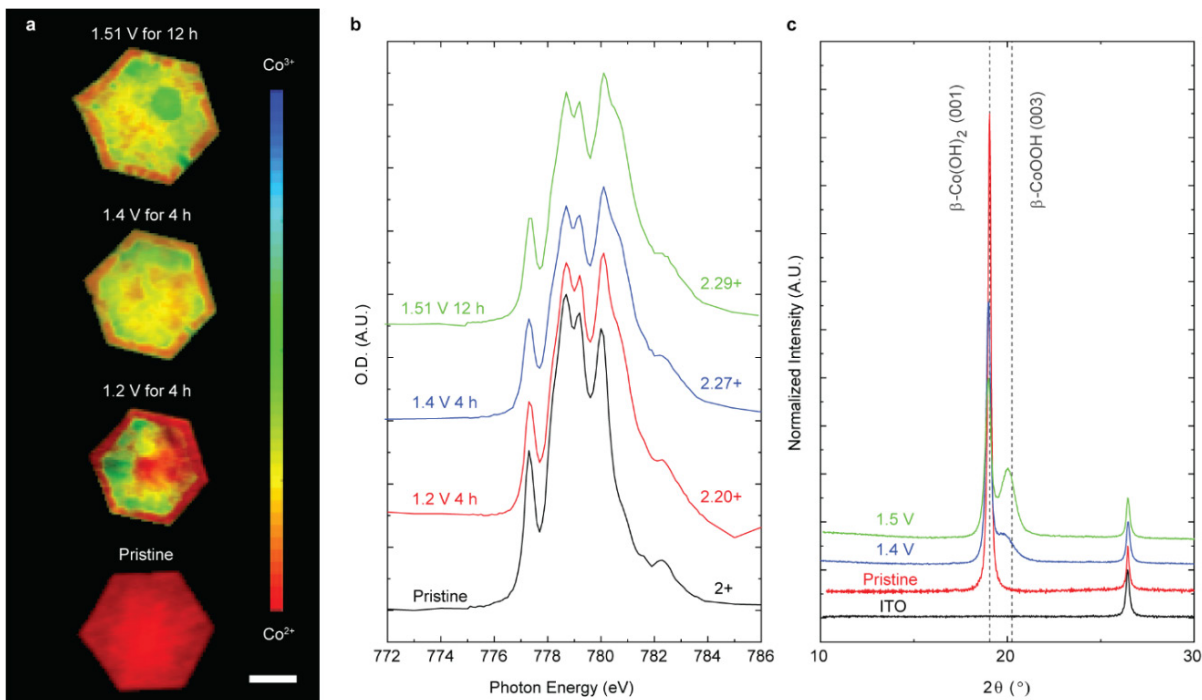


**Figure S12 | Ex-situ post-mortem analysis of  $\beta$ -Co(OH)<sub>2</sub> particles after oxidation for extended times.** (a) STXM Co oxidation state phasemaps after the electrochemical oxidation and relaxation in ambient conditions. The scale bar corresponds to 1  $\mu$ m. (b) STXM-XAS spectra averaged over all pixels for a given particle in the phasemaps in (a). (c) X-ray diffraction after 24 hours at the indicated voltage for thin-film electrode of 50  $\mu$ g cm<sup>-2</sup><sub>geom</sub>  $\beta$ -Co(OH)<sub>2</sub> on ITO coated glass.

Ex-situ post mortem analysis was performed on  $\beta$ -Co(OH)<sub>2</sub> particles after oxidation for extended periods at various voltages and then allowed to relax in ambient conditions, shown in Figure S12. STXM phasemaps, shown in Figure S12a, show that the particles preferentially relax to reduced oxidation states at the edges of the particles like the *operando* transformations observed in the main text. These reduced edge regions extend over larger length scales than what is observed under operation but demonstrate that the heterogeneity in reactivity and local chemical potential for protons in the platelet structure. It is assumed that these edge features arise after relaxation through chemical oxidation of water in the ambient air in which protons and electrons are transferred to the particles resulting in a reduction at the active region of the particles. The average oxidation state of the particles, determined through fitting the NMF end members to the STXM-XAS spectra, presented in Figure S12b, are reduced beyond what is observed during operation. The structure of the particles was measured through X-ray diffraction after oxidation at the indicated voltages for 24 hours and subsequent relaxation in ambient air, shown in Figure S12c. The results demonstrate phase separating behavior like what is observed in the relaxed STXM phasemaps. We note that there is increased intensity at lower angles, which may be correlated to amorphization or expansion of the c-axis concomitant with OH<sup>-</sup> insertion and interlayer water formation in the particles like what was observed during the *operando* EC-AFM and EQCM experiments.

## Supplemental References:

32. Suntivich, J., Gasteiger, H. A., Yabuuchi, N. & Shao-Horn, Y. Electrocatalytic Measurement Methodology of Oxide Catalysts Using a Thin-Film Rotating Disk Electrode. *J. Electrochem. Soc.* **157**, B1263–B1268 (2010).
33. Trotochaud, L., Young, S. L., Ranney, J. K. & Boettcher, S. W. Nickel–Iron Oxyhydroxide Oxygen-Evolution Electrocatalysts: The Role of Intentional and Incidental Iron Incorporation. *J. Am. Chem. Soc.* **136**, 6744–6753 (2014).
34. Stevens, M. B., Trang, C. D. M., Enman, L. J., Deng, J. & Boettcher, S. W. Reactive Fe-Sites in Ni/Fe (Oxy)hydroxide Are Responsible for Exceptional Oxygen Electrocatalysis Activity. *J. Am. Chem. Soc.* **139**, 11361–11364 (2017).
35. Gorman, C. B., Carroll, R. L., He, Y., Tian, F. & Fuierer, R. Chemically Well-Defined Lithography Using Self-Assembled Monolayers and Scanning Tunneling Microscopy in Nonpolar Organothiol Solutions. *Langmuir* **16**, 6312–6316 (2000).
36. Bentley, C. L. *et al.* Electrochemical maps and movies of the hydrogen evolution reaction on natural crystals of molybdenite (MoS<sub>2</sub>): basal vs. edge plane activity. *Chem. Sci.* **8**, 6583–6593 (2017).
37. Tao, B., Yule, L. C., Daviddi, E., Bentley, C. L. & Unwin, P. R. Correlative Electrochemical Microscopy of Li-Ion (De)intercalation at a Series of Individual LiMn<sub>2</sub>O<sub>4</sub> Particles. *Angew. Chem. Int. Ed.* **58**, 4606–4611 (2019).
38. Hill, J. W. & Hill, C. M. Directly Mapping Photoelectrochemical Behavior within Individual Transition Metal Dichalcogenide Nanosheets. *Nano Lett.* **19**, 5710–5716 (2019).
39. Snowden, M. E. *et al.* Scanning Electrochemical Cell Microscopy: Theory and Experiment for Quantitative High Resolution Spatially-Resolved Voltammetry and Simultaneous Ion-Conductance Measurements. *Anal. Chem.* **84**, 2483–2491 (2012).
40. Ebejer, N. *et al.* Scanning Electrochemical Cell Microscopy: A Versatile Technique for Nanoscale Electrochemistry and Functional Imaging. *Annual Rev. Anal. Chem.* **6**, 329–351 (2013).
41. Chen, C.-H., Meadows, K. E., Cuharuc, A., Lai, S. C. S. & Unwin, P. R. High resolution mapping of oxygen reduction reaction kinetics at polycrystalline platinum electrodes. *Phys. Chem. Chem. Phys.* **16**, 18545–18552 (2014).
42. Daviddi, E. *et al.* Nanoscale electrochemistry in a copper/aqueous/oil three-phase system: surface structure–activity–corrosion potential relationships. *Chem. Sci.* **12**, 3055–3069 (2021).
43. Bentley, C. L. *et al.* Local Surface Structure and Composition Control the Hydrogen Evolution Reaction on Iron Nickel Sulfides. *Angew. Chem. Int. Ed.* **57**, 4093–4097 (2018).
44. Wang, Y., Gordon, E. & Ren, H. Mapping the Nucleation of H<sub>2</sub> Bubbles on Polycrystalline Pt via Scanning Electrochemical Cell Microscopy. *J. Phys. Chem. Lett.* **10**, 3887–3892 (2019).
45. Deakin, M. R. & Buttry, D. A. Electrochemical applications of the quartz crystal microbalance. *Anal. Chem.* **61**, 1147A–1154A (1989).
46. Ross, F. M. *Liquid Cell Electron Microscopy*. (ed. Ross, F. M.) (Cambridge Univ. Press, Cambridge, 2016).
47. Gent, W. E. *et al.* Coupling between oxygen redox and cation migration explains unusual electrochemistry in lithium-rich layered oxides. *Nat. Commun.* **8**, 2091 (2017).
48. Liu, Y.-C., Koza, J. A. & Switzer, J. A. Conversion of electrodeposited Co(OH)<sub>2</sub> to CoOOH and Co<sub>3</sub>O<sub>4</sub>, and comparison of their catalytic activity for the oxygen evolution reaction. *Electrochim. Acta* **140**, 359–365 (2014).
49. Deng, T. *et al.* Atomic-level energy storage mechanism of cobalt hydroxide electrode for pseudocapacitors. *Nat. Commun.* **8**, 15194 (2017).
50. Pourbaix, M. *Atlas of electrochemical equilibria in aqueous solutions*. (NACE International, Houston, 1974).
51. Chivot, J., Mendoza, L., Mansour, C., Pauporté, T. & Cassir, M. New insight in the behaviour of Co–H<sub>2</sub>O system at 25–150°C, based on revised Pourbaix diagrams. *Corros. Sci.* **50**, 62–69 (2008).

52. Friebel, D. *et al.* On the chemical state of Co oxide electrocatalysts during alkaline water splitting. *Phys. Chem. Chem. Phys.* **15**, 17460–17467 (2013).
53. Liu, Z., Ma, R., Osada, M., Takada, K. & Sasaki, T. Selective and Controlled Synthesis of  $\alpha$ - and  $\beta$ -Cobalt Hydroxides in Highly Developed Hexagonal Platelets. *J. Am. Chem. Soc.* **127**, 13869–13874 (2005).
54. Kanan, M. W. & Nocera, D. G. In Situ Formation of an Oxygen-Evolving Catalyst in Neutral Water Containing Phosphate and  $\text{Co}^{2+}$ . *Science* **321**, 1072–1075 (2008).
55. Trotochaud, L., Ranney, J. K., Williams, K. N. & Boettcher, S. W. Solution-Cast Metal Oxide Thin Film Electrocatalysts for Oxygen Evolution. *J. Am. Chem. Soc.* **134**, 17253–17261 (2012).
56. Surendranath, Y., Kanan, M. W. & Nocera, D. G. Mechanistic Studies of the Oxygen Evolution Reaction by a Cobalt-Phosphate Catalyst at Neutral pH. *J. Am. Chem. Soc.* **132**, 16501–16509 (2010).
57. Boggio, R., Carugati, A. & Trasatti, S. Electrochemical surface properties of  $\text{Co}_3\text{O}_4$  electrodes. *J. Appl. Electrochem.* **17**, 828–840 (1987).
58. Hamdani, M., Singh, R. N. & Chartier, P.  $\text{Co}_3\text{O}_4$  and Co-Based Spinel Oxides Bifunctional Oxygen Electrodes. *Int. J. Electrochem. Sci.* **5**, 556–577 (2010).
59. Chen, Z. *et al.* Activity of pure and transition metal-modified  $\text{CoOOH}$  for the oxygen evolution reaction in an alkaline medium. *J. Mater. Chem. A* **5**, 842–850 (2017).
60. Zhang, M., de Respinis, M. & Frei, H. Time-resolved observations of water oxidation intermediates on a cobalt oxide nanoparticle catalyst. *Nat. Chem.* **6**, 362–367 (2014).
61. Zhang, X., Chen, Y.-S., Kamat, P. V. & Ptasinska, S. Probing Interfacial Electrochemistry on a  $\text{Co}_3\text{O}_4$  Water Oxidation Catalyst Using Lab-Based Ambient Pressure X-ray Photoelectron Spectroscopy. *J. Phys. Chem. C* **122**, 13894–13901 (2018).
62. Bergmann, A. *et al.* Reversible amorphization and the catalytically active state of crystalline  $\text{Co}_3\text{O}_4$  during oxygen evolution. *Nat. Commun.* **6**, 8625 (2015).
63. Koza, J. A., Hull, C. M., Liu, Y.-C. & Switzer, J. A. Deposition of  $\beta$ - $\text{Co}(\text{OH})_2$  Films by Electrochemical Reduction of Tris(ethylenediamine)cobalt(III) in Alkaline Solution. *Chem. Mater.* **25**, 1922–1926 (2013).
64. de Chialvo, M. R. G. & Chialvo, A. C. Oxygen evolution reaction on electrochemically generated thick cobalt oxide films. *Electrochim. Acta* **35**, 437–443 (1990).
65. Wang, H.-Y. *et al.* In Operando Identification of Geometrical-Site-Dependent Water Oxidation Activity of Spinel  $\text{Co}_3\text{O}_4$ . *J. Am. Chem. Soc.* **138**, 36–39 (2016).
66. Favaro, M. *et al.* Understanding the Oxygen Evolution Reaction Mechanism on  $\text{CoO}_x$  using Operando Ambient-Pressure X-ray Photoelectron Spectroscopy. *J. Am. Chem. Soc.* **139**, 8960–8970 (2017).
67. Tung, C.-W. *et al.* Reversible adapting layer produces robust single-crystal electrocatalyst for oxygen evolution. *Nat. Commun.* **6**, 8106 (2015).
68. Reikowski, F. *et al.* Operando Surface X-ray Diffraction Studies of Structurally Defined  $\text{Co}_3\text{O}_4$  and  $\text{CoOOH}$  Thin Films during Oxygen Evolution. *ACS Catal.* **9**, 3811–3821 (2019).
69. McAlpin, J. G. *et al.* Electronic Structure Description of a  $[\text{Co}(\text{III})_3\text{Co}(\text{IV})\text{O}_4]$  Cluster: A Model for the Paramagnetic Intermediate in Cobalt-Catalyzed Water Oxidation. *J. Am. Chem. Soc.* **133**, 15444–15452 (2011).
70. Kutin, Y., Cox, N., Lubitz, W., Schnegg, A. & Rüdiger, O. In Situ EPR Characterization of a Cobalt Oxide Water Oxidation Catalyst at Neutral pH. *Catalysts* **9**, 926 (2019).
71. Angelov, S., Zhecheva, E., Stoyanova, R. & Atanasov, M. Bulk defects in  $\text{Co}_3\text{O}_4$ , pure and slightly doped with lithium, revealed by EPR of the tetrahedral  $\text{Co}^{2+}$  ions. *J. Phys. Chem. Solids* **51**, 1157–1161 (1990).
72. Dutta, P., Seehra, M. S., Thota, S. & Kumar, J. A comparative study of the magnetic properties of bulk and nanocrystalline  $\text{Co}_3\text{O}_4$ . *J. Phys. Condens. Matter* **20**, 015218 (2007).
73. Venkateswara Rao, K. & Sunandana, C. S.  $\text{Co}_3\text{O}_4$  nanoparticles by chemical combustion: Effect of fuel to oxidizer ratio on structure, microstructure and EPR. *Solid State Commun.* **148**, 32–37 (2008).

74. Oliva, C., Forni, L. & Formaro, L. Effect of Thermal Treatment on the EPR Spectrum and on Catalytic Properties of Pure Co<sub>3</sub>O<sub>4</sub>. *Appl. Spectrosc.* **50**, 1395–1398 (1996).
75. Guggenberger, L. J., Prewitt, C. T., Meakin, P., Trofimenko, S. & Jesson, J. P. Crystal structure and single-crystal electron paramagnetic resonance data for bis[dihydrobis(1-pyrazolyl)borato]cobalt(II). *Inorg. Chem.* **12**, 508–515 (1973).
76. Macedo, R. dos S., Fazzi, R. B., Ferreira, A. M. da C. & Constantino, V. R. L. Cobalt-based layered double hydroxides revisited: evidence for oxidizing radical generation. *New J. Chem.* **44**, 10022–10032 (2020).
77. Bera, S. *et al.* Enhancing Water Oxidation Activity by Tuning Two-Dimensional Architectures and Compositions on CoMo Hydr(oxy)oxide. *J. Phys. Chem. C* **124**, 16879–16887 (2020).
78. Al-Ghoul, M., El-Rassy, H., Coradin, T. & Mokalled, T. Reaction–diffusion based co-synthesis of stable  $\alpha$ - and  $\beta$ -cobalt hydroxide in bio-organic gels. *J. Cryst. Growth* **312**, 856–862 (2010).
79. Suntivich, J., May, K. J., Gasteiger, H. A., Goodenough, J. B. & Shao-Horn, Y. A Perovskite Oxide Optimized for Oxygen Evolution Catalysis from Molecular Orbital Principles. *Science* **334**, 1383–1385 (2011).
80. Gent, W. E., Abate, I. I., Yang, W., Nazar, L. F. & Chueh, W. C. Design Rules for High-Valent Redox in Intercalation Electrodes. *Joule* **4**, 1369–1397 (2020).
81. Grimaud, A. *et al.* Oxygen Evolution Activity and Stability of Ba<sub>6</sub>Mn<sub>5</sub>O<sub>16</sub>, Sr<sub>4</sub>Mn<sub>2</sub>CoO<sub>9</sub>, and Sr<sub>6</sub>Co<sub>5</sub>O<sub>15</sub>: The Influence of Transition Metal Coordination. *J. Phys. Chem. C* **117**, 25926–25932 (2013).
82. Mefford, J. T. *et al.* Water electrolysis on La<sub>1-x</sub>Sr<sub>x</sub>CoO<sub>3- $\delta$</sub>  perovskite electrocatalysts. *Nat. Commun.* **7**, 11053 (2016).
83. Baker, M. L. *et al.* K- and L-edge X-ray absorption spectroscopy (XAS) and resonant inelastic X-ray scattering (RIXS) determination of differential orbital covalency (DOC) of transition metal sites. *Coord. Chem. Rev.* **345**, 182–208 (2017).
84. Poltavets, V. V., Croft, M. & Greenblatt, M. Charge transfer, hybridization and local inhomogeneity effects in Na<sub>x</sub>CoO<sub>2</sub>·yH<sub>2</sub>O: An x-ray absorption spectroscopy study. *Phys. Rev. B* **74**, 125103 (2006).
85. van Elp, J. *et al.* Electronic structure of CoO, Li-doped CoO, and LiCoO<sub>2</sub>. *Phys. Rev. B* **44**, 6090–6103 (1991).
86. Risch, M. *et al.* Reversibility of Ferri-/Ferrocyanide Redox during Operando Soft X-ray Spectroscopy. *J. Phys. Chem. C* **119**, 18903–18910 (2015).
87. Polo da Fonseca, C. N., De Paoli, M.-A. & Gorenstein, A. Electrochromism in cobalt oxide thin films grown by anodic electroprecipitation. *Sol. Energy Mater. Sol. Cells* **33**, 73–81 (1994).
88. Maruyama, T. & Arai, S. Electrochromic Properties of Cobalt Oxide Thin Films Prepared by Chemical Vapor Deposition. *J. Electrochem. Soc.* **143**, 1383–1386 (1996).
89. X-Ray Attenuation Length. [http://henke.lbl.gov/optical\\_constants/atten2.html](http://henke.lbl.gov/optical_constants/atten2.html).
90. Schneider, N. M. *et al.* Electron–Water Interactions and Implications for Liquid Cell Electron Microscopy. *J. Phys. Chem. C* **118**, 22373–22382 (2014).
91. Hill, M. A. & Smith, F. A. Calculation of initial and primary yields in the radiolysis of water. *Radiat. Phys. Chem.* **43**, 265–280 (1994).
92. Teo, B. K. *X-Rays and Electrons*. in *EXAFS: Basic Principles and Data Analysis* (ed. Teo, B. K.) 1–20 (Springer, Berlin, 1986)
93. Schwarz, H. A. Free radicals generated by radiolysis of aqueous solutions. *J. Chem. Educ.* **58**, 101 (1981).